Available online at www.sciencedirect.com

ScienceDirect

Geochimica et Cosmochimica Acta 295 (2021) 80–97

Geochimica et Cosmochimica Acta

www.elsevier.com/locate/gca

Nitrogen isotope fractionations among gaseous and aqueous NH_4^+, NH_3, N_2, and metal-ammine complexes: Theoretical calculations and applications

Long Li [a,*], Yuyang He [b,1], Zhe Zhang [a], Yun Liu [c,d,e]

[a] Department of Earth and Atmospheric Sciences, University of Alberta, Edmonton, Alberta T6G 2E3, Canada
[b] Institute of Mechanics, Chinese Academy of Sciences, Beijing 100190, China
[c] State Key Laboratory of Ore Deposit Geochemistry, Institute of Geochemistry, Chinese Academy of Sciences, Guiyang 550081, China
[d] Chinese Academy of Sciences Center for Excellence in Comparative Planetology, Hefei 230001, China
[e] International Center for Planetary Science, College of Earth Sciences, Chengdu University of Technology, Chengdu 610059, China

Received 29 June 2020; accepted in revised form 14 December 2020; available online 10 January 2021

Abstract

Ammonium (NH_4^+), ammonia (NH_3) and N_2 are key nitrogen species in geological nitrogen recycling. NH_3 has also been proposed to play an important role in mobilizing base metals in the form of metal-ammine complexes in hydrothermal fluids. The nitrogen isotope fractionation factors among these nitrogen species in aqueous and gaseous phases are essential parameters to trace source signatures and geochemical properties in geological processes. However, the nitrogen isotope fractionation factors for metal-ammine complexes are largely absent, and the few existing nitrogen isotope fractionation factors for the aqueous NH_4^+ – aqueous NH_3 pair show large discrepancy between experimental results and theoretical calculations. In this study, we employed the density functional theory to systematically calculate the nitrogen isotope fractionation factors among the nitrogen species that may occur in a hydrothermal system, i.e., gaseous N_2, gaseous and aqueous NH_4^+ and NH_3, and ammine complexes of Co, Zn, Cu, Cd, Ag, Au, and Pt. Based on these new results, the large nitrogen isotope fractionations for the aqueous NH_4^+ – aqueous NH_3 pair observed in previous experimental studies can be well explained by a combined effect of an equilibrium isotope fractionation between aqueous NH_4^+ and aqueous NH_3 and a kinetic isotope fractionation during NH_3 degassing from the solution. This suggests that the nitrogen isotopic behavior during NH_3 degassing in natural hydrothermal system can be more complicated than previous thought. A numeric model is thus established here to quantify the combined isotopic effect on partial NH_3 degassing. Using the new results of metal-ammine complexes, we also tested the hypothesis that nitrogen mobilization could be controlled by copper-ammine complex based on the copper concentration-$\delta^{15}N$ relationship previously observed in meta-gabbros.

Keywords: Nitrogen isotope fractionation; Ammonium; Metal-ammine complex; Ammonia degassing; Hydrothermal fluid

1. INTRODUCTION

Geological nitrogen cycle, which is commonly mediated by hydrothermal fluids (e.g., Busigny and Bebout, 2013; Li et al., 2007, 2014; Halama et al., 2010, 2017), involves transformation of various nitrogen species within or between Earth's reservoirs, e.g., the atmosphere, crust, and mantle

* Corresponding author.
E-mail address: long4@ualberta.ca (L. Li).
[1] Equal contribution.

https://doi.org/10.1016/j.gca.2020.12.010
0016-7037/

(e.g., Halama et al., 2014; Mikhail and Sverjensky, 2014; Bebout et al., 2016). In particular, the nitrogen transfer between the atmosphere, in which nitrogen occurs mainly as N_2, and the lithosphere, in which nitrogen mainly occurs as NH_4^+ substituting K^+ in mineral lattices (Honma and Itihara, 1981), may pass through an intermediate nitrogen species of NH_3 (e.g., Brandes et al., 1998; Li et al., 2007, 2009, 2014). NH_3 may also play an important role in alkaline fluids occurring in a variety of geological settings, such as the deep aquifer in ophiolites (e.g., the Oman ophiolite, the Coast Range ophiolite; see Holm et al., 2006 and reference therein), the deep subsurface fracture waters in Precambrian cratons (e.g., South Africa; Onstott et al., 2006), ridge flank hydrothermal systems (e.g., Lost City, Rainbow; see the discussion in Li et al., 2012 and reference therein), subduction zones (e.g., Mariana forearc; Wheat et al., 2008), hot spots (e.g., Yellowstone; Holloway et al., 2011), and alkaline lakes (e.g., Lake Bosumtwi, Ghana; Talbot and Johannessen, 1992). This is because NH_4^+ in alkaline fluids can be dissociated into NH_3, which can be further removed from the fluid by degassing. The relative proportions of NH_4^+, NH_3, and N_2 in hydrothermal fluid are strongly dependent on the redox and pH conditions (e.g., Duit et al., 1986; Li et al., 2012; Li and Keppler, 2014; Mikhail and Sverjensky, 2014).

Besides being a key species in geological nitrogen cycle, NH_3 may also play an important role in hydrothermal enrichment and mobilization of base metals because it is an effective ligand to form metal-ammine complexes with transition metals, such as Cu (Hathaway and Tomlinson, 1970; Han et al., 1974; Chu et al., 1978), Ni (Gupta and Sarpal, 1967), Co (Meek and Ibers, 1970), Zn (Eßmann, 1995), and Ag (Geddes and Bottger, 1969; Widmer-Cooper et al., 2001; Fox et al., 2002). This property of NH_3 has been applied in industry to recover transition metals from ore deposits (e.g., Meng and Han, 1996; Katsiapi et al., 2010). In natural hydrothermal system, a possible coupling between NH_3 and Cu has been proposed based on geochemical signatures of hydrothermally altered gabbros (Busigny et al., 2011). If NH_3 can promote the solubility and mobility of base metals in hydrothermal system, it may potentially act as an important agent for ore genesis (Irving and Williams, 1953; Martell and Hancock, 1996).

Nitrogen isotopes have been used as a robust tool to trace nitrogen remobilization (e.g., Bebout et al., 1999; Busigny et al., 2005; Li et al., 2007) and geological nitrogen recycling (e.g., Bebout and Fogel, 1992; Busigny et al., 2003; Svensen et al., 2008; Halama et al., 2010; Li et al., 2009, 2014). In order to apply nitrogen isotope system to constrain nitrogen sources and fluxes in geological nitrogen recycling pathways, the nitrogen isotope fractionation factors between involved nitrogen species are crucial prerequisite parameters. However, the nitrogen isotope fractionation factors between aqueous NH_3 and metal-ammine complexes have not been well constrained yet, despite some early efforts (e.g., Gupta and Sarpal, 1967; Ishimori, 1960a). Several previous studies (Urey, 1947; Scalan, 1958; Hanschmann, 1981; Petts et al., 2015) have investigated the equilibrium nitrogen isotope fractionations among NH_4^+, NH_3 and N_2 by theoretical calculations and given very different results. These calculations were based on vibrational frequencies of nitrogen species in gas phases. However, in natural systems, particularly in hydrothermal systems, NH_4^+ and NH_3 mostly exist in aqueous phases (hereafter referred as $NH_4^+{\cdot}nH_2O$ or $NH_{4(aqueous)}^+$, and $NH_3{\cdot}nH_2O$ or $NH_{3(aqueous)}$, respectively). One previous laboratory experimental study (Li et al., 2012) showed that, under hydrothermal condition, partial dissociation of $NH_4^+{\cdot}nH_2O$ coupled with complete degassing of the produced NH_3 induced large ^{15}N enrichments in the remaining $NH_4^+{\cdot}nH_2O$, which cannot be explained by the theoretically predicted equilibrium fractionation factors between the $NH_{4(gaseous)}^+$ - $NH_{3(gaseous)}$ pair (Urey, 1947; Scalan, 1958; Hanschmann, 1981). To solve the discrepancy between the experimental and theoretical results, Li et al. (2012) proposed that the $NH_4^+{\cdot}nH_2O$ dissociation – NH_3 degassing process involved an intermediate step that $NH_4^+{\cdot}nH_2O$ was first equilibrated with $NH_3{\cdot}nH_2O$, from which NH_3 was further exsolved and degassed (Li et al., 2012). Such a process can be described as Eq. (1):

$$NH_4{}^+{\cdot}nH_2O + OH^- \leftrightharpoons NH_3{\cdot}nH_2O + H_2O \rightarrow NH_{3(gaseous)} + (n+1)H_2O \quad (1)$$

Given that the produced $NH_3{\cdot}nH_2O$ was completely removed by NH_3 degassing in the experiments, and more importantly, the ^{15}N enrichments in the remaining $NH_4^+{\cdot}nH_2O$ apparently fitted well to a batch model assuming equilibrium isotope fractionation between $NH_4^+{\cdot}nH_2O$ and $NH_3{\cdot}nH_2O$, Li et al. (2012) interpreted the strong ^{15}N enrichments observed in the remaining $NH_4^+{\cdot}nH_2O$ as a result of large equilibrium isotope fractionations (e.g., +45.4‰ at 23 °C and + 33.5‰ at 70 °C) between $NH_4^+{\cdot}nH_2O$ and $NH_3{\cdot}nH_2O$ without considering kinetic isotopic effect from NH_3 degassing. However, a recent laboratory experimental study (Deng et al., 2018) found significant kinetic nitrogen isotopic effect (-8.2‰ at 21 °C, and −5.2‰ at 70 °C) during degassing of $NH_{3(gas)}$ from $NH_3{\cdot}nH_2O$. In addition, a recent theoretical calculation (Walters et al., 2019) using relatively simple HF/6-31G(d) and B3LYP/6-31G(d) levels of theory yielded significantly different nitrogen isotope fractionation factors between $NH_4^+{\cdot}nH_2O$ and $NH_3{\cdot}nH_2O$. Thus, it is necessary to reassess the isotopic behavior during NH_3 degassing process described by Eq. (1).

To fill these knowledge gaps, we employed theoretical calculations to determine the equilibrium isotope fractionations among gaseous N_2 and several other nitrogen species related to NH_3 in hydrothermal fluids, including NH_4^+ and NH_3 in both gaseous and aqueous phases and metal-ammine complexes of several important base metals, i.e., Co, Ni, Cu, Zn, Cd, Ag, Au, and Pt. Theoretical calculation is a robust and efficient way to estimate the equilibrium isotope fractionation factors among these species, given that they are difficult to be characterized by laboratory experiments.

2. METHOD

2.1. Equilibrium isotope fractionation theory

The equilibrium isotope fractionation factor between a species and its atomic form can be described by the β factor (Urey, 1947; Bigeleisen and Mayer, 1947). The details of the Urey-Bigeleisen-Mayer model for theoretical calculation of equilibrium isotope fractionation factor have been intensively reviewed in the literature (e.g., Richet et al., 1977; Schauble et al., 2004; Liu et al., 2010; Young et al., 2015; Dauphas and Schauble, 2016; Blanchard et al., 2017). In brief, for an isotope exchange reaction between species A and B:

$$A + B^* \rightleftharpoons A^* + B \tag{2}$$

where the species with * contain the rare isotope (i.e., ^{15}N in this case) and the ones without * contain the most abundant isotope (i.e., ^{14}N in this case). The nitrogen equilibrium isotope fractionation factor between A and B (i.e., $\alpha_{A\text{-}B}$) can be expressed as the ratio of the $^{15}\beta$ factors of A and B:

$$\alpha_{A-B} = \frac{[\,^{15}N/\,^{14}N]_A}{[\,^{15}N/\,^{14}N]_B} = \frac{^{15}\beta_A}{^{15}\beta_B} \tag{3}$$

in which the $^{15}\beta$ factors can be estimated in harmonic approximation (Richet et al., 1977; Cao and Liu, 2012) using the Urey-Bigeleisen-Mayer model (Urey, 1947; Bigeleisen and Mayer, 1947):

$$^{15}\beta = \prod_i^N \left(\frac{u_i^*}{u_i}\right)\left(\frac{e^{-u_i^*/2}}{e^{-u_i/2}}\right)\left(\frac{1-e^{-u_i}}{1-e^{-u_i^*}}\right) \tag{4}$$

$$u_i = \frac{h\nu_i}{k_B T} \tag{5}$$

in which ν_i denotes the ith harmonic vibration frequency; h denotes the Planck constant; k_B denotes the Boltzmann constant; T denotes the temperature in Kelvin; and N denotes the harmonic vibrational modes (for non-linear molecules, $N = 3n - 6$; n is the total number of atoms).

2.2. Calculation methods

Density functional theory (DFT) calculation with the Urey-Bigeleisen-Mayer equation offers a reliable approach to theoretically estimate a β factor (Liu and Tossell, 2005). It is based on quantum chemical theories to predict the optimized molecular structure of a given system and calculate its vibrational frequencies. All optimization and harmonic vibrational frequency calculations for the ground states were performed by the software Gaussian 16 (Frisch et al., 2016). All calculations have been carried out with the B3LYP exchange-correlation functional (Lee et al., 1988; Becke, 1993), which has been widely employed in vibrational frequency-related calculations (e.g., Rustad et al., 2010; Li and Liu, 2011; Eldridge et al., 2016; Zhang and Liu, 2018a,b). The 6-311++G (d,p) basis set (Frisch et al., 1984) was used for H, O, and N atoms. LANL2TZ basis set (Hay and Wadt, 1985; Roy et al., 2008) was used for Zn, Co, Cu, Ag, Au, Cd, and Pt atoms to lessen computation time yet with negligible loss of accuracy. No scaling factor was applied because the systematic errors only influence the absolute β values but are largely cancelled during the α calculations (Schauble et al., 2006; Méheut et al., 2007).

2.3. Anharmonic effect on nitrogen species

The anharmonic correction on the Urey-Bigeleisen-Mayer equation has been discussed in previous studies (Richet et al., 1977; Liu et al., 2010; Petts et al., 2015; Zhang and Liu, 2018a). One general consent is that anharmonic effect plays a greater role in vibrations involving light elements (e.g., H, B), although the magnitude of isotope fractionations caused by anharmonic effect is still under debate (Liu et al., 2010; Petts et al., 2015). To assess the magnitude of anharmonic effect on the nitrogen species in this study, we also calculated the nitrogen isotope fractionations with and without anharmonic correction for gaseous NH_4^+ and gaseous NH_3.

2.4. Solvent effect on nitrogen species

When a substance is dissolved in a solution, its weak interaction with solvent molecules can cause large uncertainty of local structural configurations, and therefore influence the estimated $^{15}\beta$ values. To assess this solvent effect, we added water molecules surrounding a target species to simulate in a realistic way the environment of an aqueous solution (e.g., Rustad et al., 2008, 2010; Zhang and Liu, 2014; He and Liu, 2015; Gao et al., 2018; Zhang and Liu, 2018a,b), using the commonly used explicit solvation modes (i.e., water-droplet method; Liu and Tossell, 2005; Li and Liu, 2011; Gao et al., 2018).

For NH_3 and NH_4^+, we built four starting cluster models with 6 water molecules as the first step. The structures were optimized to the local energy minimum with zero imaginary frequency. Subsequently, additional 6 water molecules were added to the second shell of the optimized structures and were optimized to the local energy minimum again. This process was repeated until the calculated $^{15}\beta$ value reached convergence. For the $NH_3{\cdot}nH_2O$ models, the convergence cluster has 30 water molecules. For the $NH_4^+{\cdot}nH_2O$ models, the convergence cluster has 36 water molecules.

For dissolved metal-ammine complexes, the solvent effect was also assessed (using $Zn(NH_3)_6^{2+}$ and $Ni(NH_3)_6^{2+}$ as examples), following previous studies (e.g., Rudolph et al., 2000; Hill and Schauble, 2008) by adding a hydration sphere ($12H_2O$) on the studied molecular cluster.

3. RESULTS

3.1. Anharmonic effect on isotope fractionation between gaseous NH_4^+ and NH_3

The results of harmonic vibrational frequencies (w_i) and anharmonicity constants (x_{ij}) for NH_3 and NH_4^+ are listed in Table 1. Comparison between the $\ln\alpha_{NH_{4\,(gaseous)}^+ - NH_{3\,(gaseous)}}$ results with and without anharmonic corrections indicates

Table 1
Harmonic vibrational frequencies (ω_i) and anharmonicity constants (x_{ij}) for NH_3 and NH_4^+.

	$^{14}NH_3$	$^{15}NH_3$		$^{14}NH_4^+$	$^{15}NH_4^+$
w_1	1005.6647	1000.2964	w_1	1489.3992	1482.4191
w_2	1668.9006	1665.5001	w_2	1489.5274	1482.5471
w_3	1668.9599	1665.5593	w_3	1489.5677	1482.5874
w_4	3480.3335	3478.3005	w_4	1727.4986	1727.4986
w_5	3607.0377	3597.1959	w_5	1727.5563	1727.5563
w_6	3607.3700	3597.5267	w_6	3371.2896	3371.2895
x_{11}	−44.5655	−44.0991	w_7	3474.2659	3464.5960
x_{12}	−7.4656	−7.3437	w_8	3474.6356	3464.9637
x_{13}	−60.6278	−60.1753	w_9	3474.9376	3465.2644
x_{14}	−99.6980	−99.5133	x_{11}	−35.9750	−35.6432
x_{15}	−15.1020	−14.9203	x_{12}	4.9813	4.8697
x_{16}	25.8310	25.4004	x_{13}	−63.5821	−63.4649
x_{22}	−6.8370	−12.9044	x_{14}	−16.5959	−16.4789
x_{23}	−14.9178	−14.7277	x_{15}	−11.3300	−11.2686
x_{24}	−22.0048	2.4055	x_{16}	−11.1957	−11.0121
x_{25}	−12.3932	−12.4064	x_{17}	−68.8225	−68.4742
x_{26}	−14.9338	−15.0119	x_{18}	−13.5188	−13.3919
x_{33}	−44.2150	−43.7427	x_{19}	−11.9319	−11.9304
x_{34}	−99.6208	−99.4716	x_{22}	−35.9787	−35.6468
x_{35}	−7.3950	−7.2582	x_{23}	−64.3850	−64.3460
x_{36}	26.1471	25.7100	x_{24}	−16.6125	−16.4950
x_{44}	−26.5479	−26.5878	x_{25}	−11.1808	−10.9972
x_{45}	−21.9967	2.2832	x_{26}	−11.3447	−11.2835
x_{46}	18.0323	18.1441	x_{27}	−68.0429	−67.6153
x_{55}	−6.8509	−12.8954	x_{28}	−13.5173	−13.3903
x_{56}	−14.7680	−14.8366	x_{29}	−11.9177	−11.9169
x_{66}	−61.1998	−60.5714	x_{33}	−15.9055	−15.9056
			x_{34}	−23.4745	−23.4746
			x_{35}	−4.8519	−5.3443
			x_{36}	−4.9011	−5.3913
			x_{37}	−63.9414	−63.8669
			x_{38}	−23.4652	−23.4654
			x_{39}	−4.8868	−5.3762
			x_{44}	−1.6234	−1.6235
			x_{45}	−3.5137	−3.5376
			x_{46}	−3.5439	−3.5675
			x_{47}	−12.0062	−11.8748
			x_{48}	−3.4073	−3.4073
			x_{49}	−18.4950	−18.4922
			x_{55}	−6.7531	−6.5817
			x_{56}	4.4641	4.5306
			x_{57}	−11.9000	−11.9027
			x_{58}	−13.4279	−13.4342
			x_{59}	−6.1422	−5.8856
			x_{66}	−6.7632	−6.5921
			x_{67}	−11.8785	−11.8801
			x_{68}	−13.4427	−13.4488
			x_{69}	−6.1608	−5.9043
			x_{77}	−17.5888	−17.3853
			x_{78}	−18.0933	−17.9816
			x_{79}	−10.6254	−10.3797
			x_{88}	−1.6219	−1.6220
			x_{89}	1.3786	1.3461
			x_{99}	−4.1523	−4.0280
ZPE_{harm}	**7519.1332**	**7502.1895**	**ZPE_{harm}**	**10859.3390**	**10834.3611**
ZPE_{anh}	**7394.8057**	**7378.5208**	**ZPE_{anh}**	**10683.4961**	**10659.4508**

that anharmonic effect on $\ln\alpha_{NH_4^+_{(gaseous)}-NH_{3(gaseous)}}$ is small, i.e., −1.4‰ at 0 °C, −0.6‰ at 400 °C, and −0.3‰ at 1000 °C (Table 2). Therefore, we did not apply the anharmonic corrections for the other nitrogen species in this study. For consistency, we used all the harmonic results to calculate the $1000\ln\alpha$ values.

Table 2
$\ln\alpha_{NH4+(gaseous)\ -\ NH3(gaseous)}$ for harmonic and anharmonic calculations at 0–1000 °C.

T (°C)	Harmonic	Anharmonic
0	35.2	33.8
20	32.4	31.0
40	29.8	28.5
60	27.5	26.4
80	25.5	24.4
100	23.8	22.7
200	17.3	16.5
400	10.2	9.6
600	6.7	6.2
800	4.7	4.4
1000	3.6	3.3

3.2. Isotope fractionations between NH_4^+ and NH_3 in gaseous and aqueous phases

Fig. 1 illustrates the optimized geometries for gaseous NH_3 and NH_4^+, and their aqueous phases represented by $NH_3{\cdot}30H_2O$ and $NH_4^+{\cdot}36H_2O$, respectively. The coordinates of these optimized geometries are listed in the Supplementary Data. Our calculations yielded the N-H bond length and H-N-H bond angle as 1.01(4) Å and 107.9°, respectively, for gaseous NH_3, and 1.02(6) Å and 109.5°, respectively, for gaseous NH_4^+. These values are consistent with previous theoretical calculation and experimental results, e.g., 1.01(2) Å for the N-H bond length and 106.67° for the H-N-H bond angle in gaseous NH_3 (Haynes, 2014), and 1.02(7) Å for the N-H bond length and 109.5° for the H-N-H bond angle in gaseous NH_4^+ (Chen and Davidson 2001). The NH_3 molecule is hydrated in all explicit solvent models, in which N forms a 1.65–1.69 Å hydrogen bond with H of a water molecule.

Table 3 lists the calculated $^{15}\beta$ results of NH_3 and NH_4^+ in gaseous phases as well as aqueous phases hydrated by 6–30 H_2O molecules in 4 different configurations at 25 °C. The results show that the $^{15}\beta$ values increase significantly from gaseous NH_3 ($^{15}\beta = 1.0687$) to hydrated NH_3, whose $^{15}\beta$ values vary strongly with an increase in the surrounding H_2O molecule numbers until converge at 1.0776 when the H_2O molecule number reaches 30. This solvent effect results in large equilibrium isotope fractionations between $NH_{3(aqueous)}$ and $NH_{3(gaseous)}$ (e.g., $\ln\alpha_{NH_{3(aqeous)}-NH_{3(gaseous)}} = +8.3‰$ at 25 °C). In contrast, the $^{15}\beta$ value of NH_4^+ is not significantly shifted after hydration (Table 3), resulting in negligible isotope fractionation between gaseous and aqueous NH_4^+, e.g., the $\ln\alpha_{NH_{4(aqeous)}^+-NH_{4(gaseous)}^+}$ value is +0.3‰ at 25 °C, and mostly within the calculation uncertainty of ±0.5% at other temperatures (Tables 4–5). Therefore, we will not specifically distinguish between aqueous and gaseous NH_4^+ in the discussions below.

The 1000lnβ values at selected temperatures are given in Table 4, and the general equations describing the temperature-dependent $^{15}\beta$ values for individual species are given in Table 5 and plotted in Fig. 3. The temperature-dependent equilibrium isotope fractionations

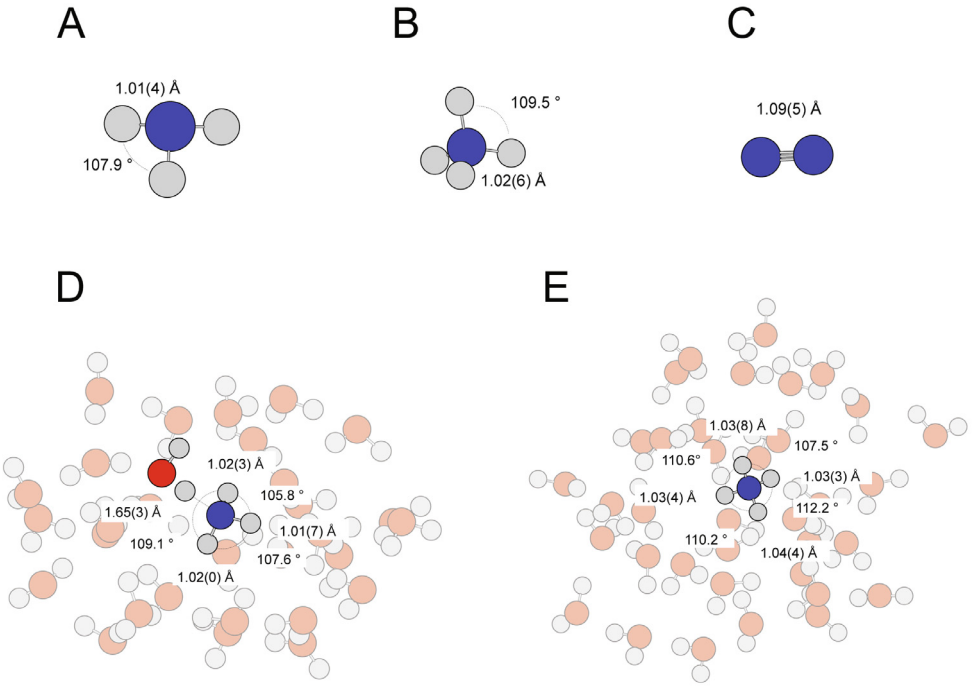

Fig. 1. Optimized geometries for gaseous NH_3 (A), NH_4^+ (B), N_2 (C), and representative local configuration of $NH_3{\cdot}30H_2O$ (D) and $NH_4^+{\cdot}36H_2O$ (E).

Table 3
Calculated $^{15}\beta$ factors ($^{15}N/^{14}N$) of ammonia and ammonium in gaseous and aqueous phases at B3LYP/6-311G++(d,p) level at 25 °C.

Species	$^{15}\beta$	1000ln$^{15}\beta$		$^{15}\beta$	1000ln$^{15}\beta$
Gaseous phase					
NH_3	1.0687	66.4	NH_4^+	1.1031	98.1
Aqueous phase					
$NH_3(H_2O)_6$_A	1.0766	73.8	$NH_4(H_2O)_6^+$_A	1.1032	98.2
$NH_3(H_2O)_6$_B	1.0767	73.9	$NH_4(H_2O)_6^+$_B	1.1038	98.8
$NH_3(H_2O)_6$_C	1.0757	73.0	$NH_4(H_2O)_6^+$_C	1.1038	98.8
$NH_3(H_2O)_6$_D	1.0786	75.7	$NH_4(H_2O)_6^+$_D	1.1039	98.8
Average*	1.0769 ± 0.0011	74.1 ± 1.0	**Average**	1.1037 ± 0.0003	98.6 ± 0.3
$NH_3(H_2O)_{12}$_A	1.0799	76.9	$NH_4(H_2O)_{12}^+$_A	1.1032	98.2
$NH_3(H_2O)_{12}$_B	1.0766	73.8	$NH_4(H_2O)_{12}^+$_B	1.1034	98.4
$NH_3(H_2O)_{12}$_C	1.0781	75.2	$NH_4(H_2O)_{12}^+$_C	1.1032	98.2
$NH_3(H_2O)_{12}$_D	1.0781	75.2	$NH_4(H_2O)_{12}^+$_D	1.1035	98.5
Average	1.0782 ± 0.0012	75.3 ± 1.1	**Average**	1.1033 ± 0.0001	98.3 ± 0.1
$NH_3(H_2O)_{18}$_A	1.0787	75.8	$NH_4(H_2O)_{18}^+$_A	1.1039	98.8
$NH_3(H_2O)_{18}$_B	1.0781	75.2	$NH_4(H_2O)_{18}^+$_B	1.1031	98.1
$NH_3(H_2O)_{18}$_C	1.0778	74.9	$NH_4(H_2O)_{18}^+$_C	1.1039	98.8
$NH_3(H_2O)_{18}$_D	1.0762	73.4	$NH_4(H_2O)_{18}^+$_D	1.1026	97.7
Average	1.0777 ± 0.0009	74.8 ± 0.9	**Average**	1.1034 ± 0.0006	98.4 ± 0.5
$NH_3(H_2O)_{24}$_A	1.0776	74.7	$NH_4(H_2O)_{24}^+$_A	1.1039	98.8
$NH_3(H_2O)_{24}$_B	1.0778	74.9	$NH_4(H_2O)_{24}^+$_B	1.1041	99.0
$NH_3(H_2O)_{24}$_C	1.0776	74.7	$NH_4(H_2O)_{24}^+$_C	1.1042	99.1
$NH_3(H_2O)_{24}$_D	1.0773	74.5	$NH_4(H_2O)_{24}^+$_D	1.1035	98.5
Average	1.0776 ± 0.0002	74.7 ± 0.2	**Average**	1.1039 ± 0.0003	98.9 ± 0.2
$NH_3(H_2O)_{30}$_A	1.0771	74.3	$NH_4(H_2O)_{30}^+$_A	1.1032	98.2
$NH_3(H_2O)_{30}$_B	1.0777	74.8	$NH_4(H_2O)_{30}^+$_B	1.1044	99.3
$NH_3(H_2O)_{30}$_C	1.0780	75.1	$NH_4(H_2O)_{30}^+$_C	1.1037	98.7
$NH_3(H_2O)_{30}$_D	1.0776	74.7	$NH_4(H_2O)_{30}^+$_D	1.1028	97.9
Average	1.0776 ± 0.0003	74.7 ± 0.3	**Average**	1.1035 ± 0.0006	98.5 ± 0.5
			$NH_4(H_2O)_{36}^+$_A	1.1028	97.9
			$NH_4(H_2O)_{36}^+$_B	1.1030	98.0
			$NH_4(H_2O)_{36}^+$_C	1.1034	98.4
			$NH_4(H_2O)_{36}^+$_D	1.1031	98.1
			Average	1.1031 ± 0.0002	98.1 ± 0.2
Preferred value**	1.0776	74.7	Preferred value**	1.1035	98.5

* The "Average" data in bold are the mean values of 4 configurations (i.e., configurations A,B, C, and D).
** The preferred $^{15}\beta$ value of aqueous $NH_3(H_2O)_n$ are the average results of 8 configurations ($4 \times NH_3(H_2O)_{24}$ and $4 \times NH_3(H_2O)_{30}$), and the preferred $^{15}\beta$ value of $NH_4(H_2O)_n^+$ are the average results of 12 configurations ($4 \times NH_4(H_2O)_{24}^+$, $4 \times NH_4(H_2O)_{30}^+$, and $4 \times NH_4(H_2O)_{36}^+$).

between species are given in Table 6 and plotted in Fig. 4. It is noted that the different solvent effects on NH_4^+ and NH_3 result in much larger isotope fractionation in the $NH_{4(aqueous)}^+ - NH_{3(gaseous)}$ pair (e.g., +32.1‰ at 25 °C) than the $NH_{4(aqueous)}^+ - NH_{3(aqueous)}$ pair (e.g., +23.8‰ at 25 °C).

3.3. Isotope fractionations between NH_4^+ and N_2

The optimized geometry of gaseous N_2 is also shown in Fig. 1. Our calculations yielded the N-N bond length as 1.09(5) Å, which is consistent with previous published data (e.g., 1.0975 Å; Sutton and Bowen, 1958).

The calculated 1000lnβ results at selected temperatures are listed in Table 4 with a general description equation given in Table 5. The results show that N_2 is more enriched in ^{15}N than both gaseous and aqueous NH_3, but more depleted in ^{15}N than gaseous and aqueous NH_4^+ (Table 4). Given that experimental studies have demonstrated that the isotope fractionation between gaseous N_2 and dissolved N_2 is very small (<1‰ at 0 °C; Klots and Benson, 1963), our results of gaseous N_2 can also be approximately used for aqueous N_2. Accordingly, our calculation results self-consistently put aqueous N_2 in the right ^{15}N enrichment order between aqueous NH_3 and aqueous NH_4^+.

3.4. Metal – ammine complexes

The geometries of metal-ammine complexes are still not well constrained. In this study, we select the complex structure of the minimum-energy level from previous studies as the dominant metal-ammine complex species (see below). The optimized geometries are shown in Fig. 2, and their coordinates are listed in the Supplementary Data. The calculated $^{15}\beta$ values at selected temperatures are listed in Table 4 with general description equations being listed in Table 5. A brief summary for each metal is given below.

Zinc-ammine complexes $Zn(NH_3)_n^{2+}$ (n = coordination number) with n values varying from 4 to 6 have been reported (Kim et al., 1993; Fatmi et al., 2006; Fatmi et al., 2010). However, our calculations only obtained

Table 4
The equilibrium isotope fractionation (1000ln $^{15}\beta$) for different metal-ammine complexes at temperatures from 273–1273 K.

T (°C)	N_2 (gas)	NH_3 (gas)	NH_3 (aq)	NH_4^+ (gas)	NH_4^+ (aq)	Metal – ammine complexes*									
						Zn^{2+} (6)	Ni^{2+} (6)	Co^{2+} (6)	Co^{3+} $(6)^H$	Co^{3+} $(6)^L$	Cd^{2+} (6)	Cd^{2+} (4)	Cu^{2+} (4)	Cu^+ (4)	Ag^+ (2)	Au^+ (2)	Pt^+ (2)
0	90.9	73.9	83.5	109.1	110.1	84.3	86.9	85.5	87.6	97.2	82.8	86.4	90.9	94.0	89.6	98.2	98.7
20	83.6	67.8	76.4	100.2	100.7	77.1	79.3	78.1	80.0	88.5	75.7	78.8	82.9	85.7	81.8	89.4	89.7
40	77.1	62.6	70.2	92.4	92.5	70.7	72.8	71.7	73.4	81.0	69.6	72.4	76.0	78.5	75.0	81.9	82.1
60	71.5	58.0	64.7	85.5	85.4	65.3	67.1	66.1	67.6	74.5	64.2	66.7	70.0	72.2	69.1	75.3	75.6
80	66.5	53.9	60.0	79.5	79.2	60.5	62.1	61.3	62.6	68.8	59.5	61.8	64.8	66.7	63.9	69.5	69.7
100	62.0	50.3	55.8	74.1	73.6	56.2	57.7	56.9	58.1	63.7	55.3	57.4	60.1	61.9	59.4	64.4	64.7
200	45.5	36.9	40.4	54.2	53.3	40.8	41.7	41.2	41.9	45.6	40.2	41.5	43.3	44.4	42.9	46.1	46.2
400	27.3	22.6	24.4	32.9	32	24.5	25.0	24.8	25.1	27.0	24.3	24.9	25.9	26.4	25.7	27.3	27.4
600	18.0	15.4	16.4	22.1	21.3	16.5	16.8	16.6	16.7	17.9	16.3	16.7	17.3	17.6	17.2	18.1	18.1
800	12.7	11.0	11.7	15.8	15.1	11.7	11.9	11.8	11.9	12.7	11.6	11.9	12.2	12.5	12.2	12.9	12.9
1000	9.4	8.3	8.7	11.8	11.2	8.8	9.0	8.9	8.9	9.5	8.7	8.9	9.2	9.4	9.2	9.7	9.7

* Numbers in parentheses below each metal denotes the coordination number of NH_3. H and L in Co^{3+} denote high spin state (multiplicity = 5) and low spin states (multiplicity = 1), respectively.

meaningful results for the 6-coordinated complex Zn $(NH_3)_6^{2+}$ with a multiplicity of 1. The Zn-N bond length in the yielded geometry is 2.31 Å, which is close to the previously suggested value of 2.291 Å (Kim et al., 1993). The yielded $^{15}\beta$ is 1.0783 for $Zn(NH_3)_6^{2+}$ at 25 °C. The $^{15}\beta$ value shows an insignificant increase with hydration, to 1.0788 for $Zn(NH_3)_6^{2+}\cdot 6H_2O$, and 1.0792 for $Zn(NH_3)_6^{2+}\cdot 12H_2O$ at 25 °C.

Nickel-ammine complex can display various geometries with coordination numbers varying from 4 to 6. In this study, we focus on the 6-coordinated complex $Ni(NH_3)_6^{2+}$ with a multiplicity of 3, which is considered to be more stable (e.g., Paul et al., 2004; Varadwaj et al., 2008; Casanova and Head-Gordon, 2009; Varadwaj et al., 2009). The yielded Ni-N bond length of $Ni(NH_3)_6^{2+}$ is 2.20 Å, which is consistent with the previously suggested value of 2.205 Å and close to the crystallographically observed mean value of 2.135 Å (Varadwaj et al., 2008). The calculated $^{15}\beta$ value is 1.0807 for $Ni(NH_3)_6^{2+}$ at 25 °C, which slightly increases to 1.0817 when an additional hydration sphere of 12 H_2O is added (i.e., Ni $(NH_3)_6^{2+}\cdot 12H_2O$).

Cobalt can complex with NH_3 at valence states of II and III. The optimized structures of the complexes are 6-coordinated $Co(NH_3)_6^{2+}$ and $Co(NH_3)_6^{3+}$ (Barnet et al., 1966; Meek and Ibers, 1970; Müller and Kraus, 2015). Co $(NH_3)_6^{2+}$ is believed to be more stable at high-spin state (Schmiedekamp et al., 2002) and thus has a multiplicity of 4. While $Co(NH_3)_6^{3+}$ has been considered as a low-spin complex (e.g., Williams, 1979) and thus has a multiplicity of 1, our single-atom test yielded the lowest energy of Co^{3+} at high-spin state with a multiplicity of 5. Therefore, we reported the results of both low- and high-spin states for Co^{3+} here. Our calculation gave an average Co-N bond length of 2.26 Å for $Co(NH_3)_6^{2+}$, which is close to previously published data of 2.257–2.264 Å (Schmiedekamp et al., 2002; Varadwaj and Marques, 2010). The yielded $^{15}\beta$ value of $Co(NH_3)_6^{2+}$ is 1.0794 at 25 °C. The Co-N bond length for $Co(NH_3)_6^{3+}$ is 2.03 Å at low-spin state, which is consistent with previously calculation results (2.033 Å; Rotzinger, 2009), but increases to 2.20 Å at high-spin state. This results in a large difference in the $^{15}\beta$ values, e.g., 1.0814 at low-spin state and 1.0904 at high-spin state at 25 °C.

Cadmium-ammine complex is considered to be the stable in both 4-coordinated (i.e., $Cd(NH_3)_4^{2+}$; multiplicity = 1) and 6-coordinated (i.e., $Cd(NH_3)_6^{2+}$; multiplicity = 2) forms (Nilsson et al., 2007; Zeng et al., 2015). The yielded Cd-N bond lengths are 2.35 Å for Cd $(NH_3)_4^{2+}$, which is higher than the value of 2.02 Å reported by Zeng et al. (2015), and 2.48 Å for $Cd(NH_3)_6^{2+}$, which is higher than the value of 2.35 Å reported by Nilsson et al. (2007). The calculated $^{15}\beta$ values at 25 °C are 1.0802 for $Cd(NH_3)_4^{2+}$ and 1.0769 for $Cd(NH_3)_6^{2+}$.

Copper can complex with NH_3 at valence states of I and II. The 4-coordinated Cu(II)-ammine complex is suggested to be more stable than the 5- and 6-coordinated complexes (Pavelka and Burda, 2005). For the 4-coordinated Cu $(NH_3)_4^{2+}$ (multiplicity = 2), the calculated structure has a Cu-N bond length of 2.07 Å, which is consistent with exper-

Table 5
Polynomial fit parameters of calculated $^{15}\beta$ factors in the form of $1000 \cdot \ln(^{15}\beta) = C_0 + C_1{*}10^{-1}x - C_2{*}10^{-2}x^2 + C_3 10^{-3}x^3 - C_4{*}10^{-4}x^4 + C_5{*}10^{-5}x^5 - C_6 10^{-6}x^6$ in which $x = 10^6/T^2$ and T is temperature in Kelvin (valid from 273 to 1273 K).

Compound	C_0	C_1	C_2	C_3	C_4	C_5	C_6
$N_{2(gaseous)}$	0.27	160.78	230.62	319.21	285.31	140.65	28.766
$NH_{3(gaseous)}$	0.65	137.43	238.30	383.41	373.46	191.98	39.882
$NH_{3(aqueous)}$	0.75	142.11	214.55	315.96	286.52	139.19	27.668
$NH^+_{4(gaseous)}$	1.13	189.79	280.17	400.11	360.31	176.23	35.521
$NH^+_{4(aqueous)}$	0.51	190.47	299.05	465.60	448.62	230.51	48.098
$Zn(NH_3)_6^{2+}$	0.74	142.77	216.00	323.78	300.98	150.18	30.635
$Ni(NH_3)_6^{2+}$	0.84	143.69	208.87	305.13	277.40	135.51	27.075
$Co(NH_3)_6^{2+}$	0.77	143.52	215.04	321.63	298.11	148.06	30.022
$Co(NH_3)_6^{3+}$ (H)*	0.79	144.13	209.51	308.78	282.83	138.96	27.903
$Co(NH_3)_6^{3+}$ (L)*	0.70	154.72	216.85	318.04	291.16	143.41	28.932
$Cd(NH_3)_6^{2+}$	0.66	142.64	219.61	326.76	298.19	145.28	28.875
$Cd(NH_3)_4^{2+}$	0.83	142.65	203.83	289.48	254.75	120.34	23.266
$Cu[(NH_3)_4]^{2+}$	0.73	148.83	212.48	301.05	260.08	119.14	22.149
$Cu[(NH_3)_2]^{+}$	0.70	153.55	229.98	355.89	339.85	172.99	35.831
$Ag(NH_3)_2^{2+}$	0.85	147.16	212.91	313.78	290.42	145.54	29.982
$Au(NH_3)_2^{2+}$	0.97	152.43	197.47	263.92	217.27	95.08	16.882
$Pt(NH_3)_2^{2+}$	0.85	154.95	211.42	302.56	268.89	127.71	24.704

* H and L in $Co(NH_3)_6^{3+}$ denote high spin state (multiplicity = 5) and low spin states (multiplicity = 1), respectively.

Table 6
Parameters in the general equations for temperature-dependent equilibrium nitrogen isotope fractionations ($1000\ \ln\alpha = A \times 10^6/T^2 + B \times 10^3/T + C$; T is in Kelvin, valid in the range of 273–1273 K) of various NH_3-related species relative to $NH_{3(gaseous)}$, $NH_{3(aqueous)}$, and $NH^+_{4(aqueous)}$, respectively.

	$-NH_{3(gaseous)}$			$-NH_{3(aqueous)}$			$-NH^+_{4(aqueous)}$		
	A	B	C	A	B	C	A	B	C
$N_{2(gaseous)}$	−0.054	5.906	−3.78	−0.628	5.229	−3.30	−0.941	−1.850	0.16
$NH_{3(gaseous)}$	0	0	0	−0.574	−0.678	0.48	−0.887	−7.756	3.94
$NH_{3(aqueous)}$	0.574	0.678	−0.48	0	0	0	−0.314	−7.078	3.46
$NH^+_{4(gaseous)}$	0.409	9.361	−4.34	−0.165	8.684	−3.87	−0.478	1.605	−0.40
$NH^+_{4(aqueous)}$	0.887	7.756	−3.94	0.314	7.078	−3.46	0	0	0
$Zn(NH_3)_6^{2+}$	0.611	0.771	−0.56	0.038	0.094	−0.08	−0.276	−6.985	3.38
$Ni(NH_3)_6^{2+}$	0.748	0.997	−0.67	0.174	0.320	−0.19	−0.140	−6.759	3.27
$Co(NH_3)_6^{2+}$	0.683	0.858	−0.60	0.109	0.180	−0.12	−0.205	−6.898	3.34
$Co(NH_3)_6^{3+}$ (H)*	0.824	0.956	−0.71	0.250	0.279	−0.24	−0.064	−6.800	3.22
$Co(NH_3)_6^{3+}$ (L)*	1.293	2.044	−1.36	0.719	1.367	−0.89	0.406	−5.711	2.57
$Cd(NH_3)_6^{2+}$	0.510	0.707	−0.52	−0.064	0.030	−0.04	−0.378	−7.049	3.42
$Cd(NH_3)_4^{2+}$	0.720	0.968	−0.68	0.146	0.291	−0.21	−0.168	−6.788	3.26
$Cu(NH_3)_4^{2+}$	0.954	1.437	−0.95	0.381	0.760	−0.47	0.067	−6.319	2.99
$Cu(NH_3)_2^{+}$	1.138	1.660	−1.05	0.564	0.982	−0.57	0.250	−6.096	2.89
$Ag(NH_3)_2^{+}$	0.856	1.406	−0.86	0.282	0.729	−0.39	−0.032	−6.350	3.08
$Au(NH_3)_2^{+}$	1.321	2.212	−1.35	0.747	1.534	−0.88	0.434	−5.544	2.59
$Pt(NH_3)_2^{+}$	1.359	2.192	−1.36	0.785	1.515	−0.88	0.471	−5.563	2.58

* H and L in $Co(NH_3)_6^{3+}$ denote high spin state (multiplicity = 5) and low spin states (multiplicity = 1), respectively.

imentally determined value of 2.00 Å (Valli et al., 1996). The calculated $^{15}\beta$ value for $Cu(NH_3)_4^{2+}$ is 1.0845 under 25 °C. For Cu(I)-ammine complex, the setup structure was adopted from Pavelka and Burda (2005) as a 2-coordinated complex $Cu(NH_3)_2^+$ (multiplicity = 1). The yielded Cu-N bond length is 1.94 Å, which is consistent with the result (1.91 Å) of Pavelka and Burda (2005). The yielded $^{15}\beta$ value for $Cu(NH_3)_2^+$ is 1.0874 at 25 °C.

For the silver-ammine complex, previous studies have suggested a linearly 2-coordinated complex $Ag(NH_3)_2^+$ (multiplicity = 1) to be the most stable form (Geddes and Bottger, 1969; Shoeib et al., 2000; Widmer-Cooper et al., 2001; Fox et al., 2002). Our calculation gave the Ag-N bond length of $Ag(NH_3)_2^+$ as 2.17 Å, which is close to previously reported data (2.18 Å; Shoeib et al., 2001). The calculated $^{15}\beta$ value for $Ag(NH_3)_2^+$ is 1.0833 at 25 °C.

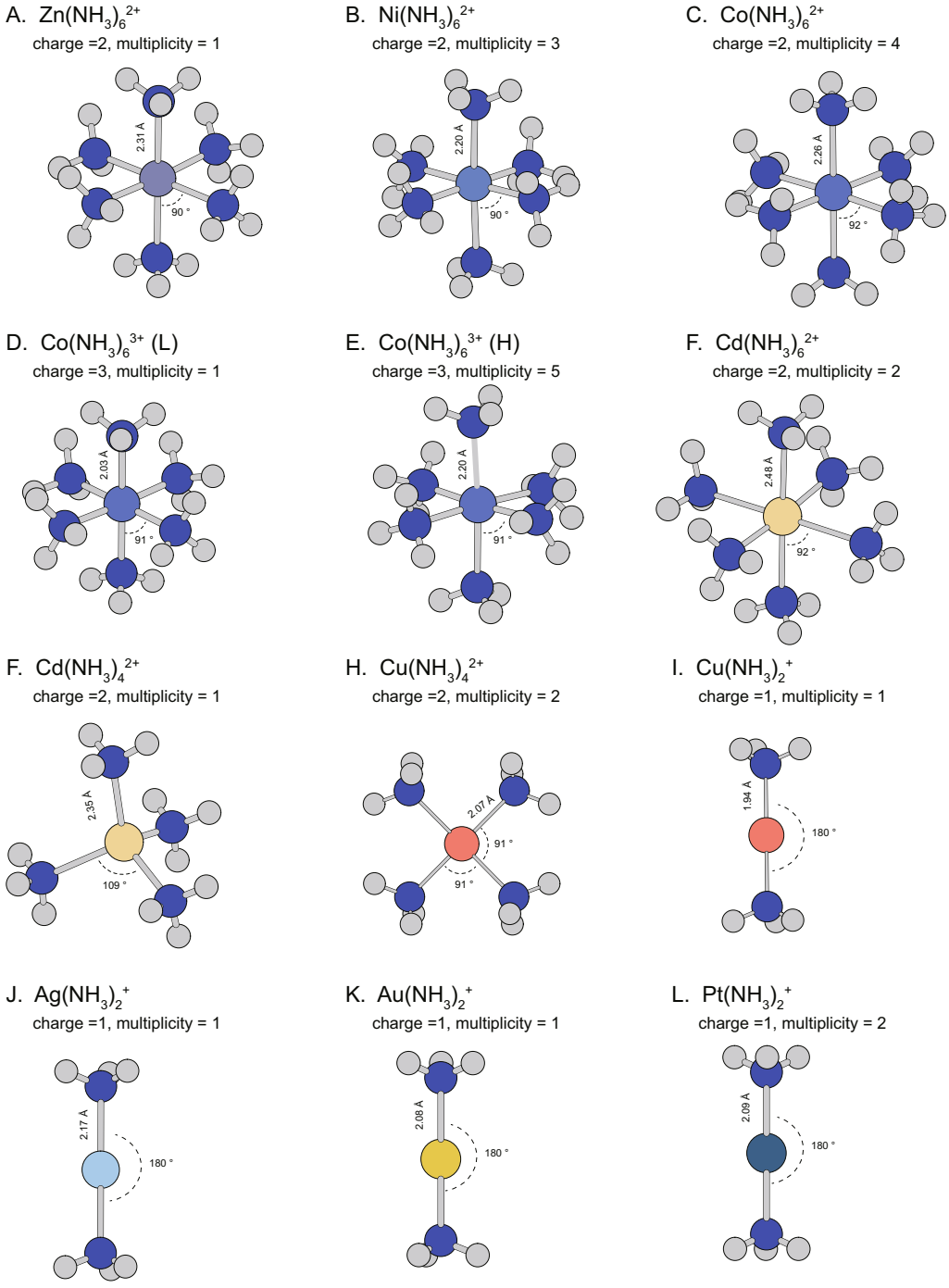

Fig. 2. Optimized geometries of $Zn(NH_3)_6^{2+}$ (A), $Ni(NH_3)_6^{2+}$ (B), $Co(NH_3)_6^{2+}$ (C), $Co(NH_3)_6^{3+}$ at low-spin state (D) or high-spin state (E), $Cd(NH_3)_6^{2+}$ (F), $Cd(NH_3)_4^{2+}$ (H), $Cu(NH_3)_2^{+}$ (I), $Ag(NH_3)_2^{+}$ (J), $Au(NH_3)_2^{+}$ (K), and $Pt(NH_3)_2^{+}$ (L).

For the gold-ammine complex, previous studies have also suggested the linearly 2-coordinated complex $Au(NH_3)_2^{+}$ (multiplicity = 1) to be most stable (Kryachko and Remacle, 2007). Our calculation gave the Au-N bond length as 2.08 Å, which is the same with the data reported by Kryachko and Remacle (2007). The calculated $^{15}\beta$ value for $Au(NH_3)_2^{+}$ is 1.0914 at 25 °C.

For the platinum-ammine complex, we also calculated the linearly 2-coordinated complex $Pt(NH_3)_2^{+}$ (multiplicity = 2), which is considered to be the most stable form (Juhász et al., 2012). The results gave the Pt-N bond length as 2.09 Å, which is close to the value of 2.07 Å reported by Juhász et al. (2012). The calculated $^{15}\beta$ value for $Pt(NH_3)_2^{+}$ is 1.0917 at 25 °C.

The equilibrium nitrogen isotope fractionations of these metal-ammine complexes relative to $NH_{3(gaseous)}$, $NH_{3(aqueous)}$, $NH_{4\,(aqueous)}^{+}$ are given in Table 6 and plotted in Fig. 3.

4. DISCUSSION

4.1. Factors controlling the N isotope fractionations in the NH_4^+ – NH_3 – metal-ammine complex system

Fig. 3 shows that ^{15}N is most enriched in NH_4^+ and most depleted in $NH_{3(gaseous)}$. This is consistent with a more stable tetrahedral structure of NH_4^+ relative to the pyramidal structure of NH_3. The hydration of NH_3 induces significant ^{15}N enrichment in $NH_{3(aqueous)}$ relative to $NH_{3(gaseous)}$, because of the additional N-H bond formed in $NH_{3(aqueous)}$ (Fig. 1). However, the hydration of $NH_{4(gaseous)}^+$ does not cause much more ^{15}N enrichment in $NH_{4(aqueous)}^+$ (+0.4‰; Table 3), because the bonding environment does not change significantly for the N in NH_4^+ (Fig. 1). Similarly, hydration of ammine complexes of Zn^{2+} (from $Zn(NH_3)_6^{2+}$ to $Zn(NH_3)_6^{2+}{\cdot}12H_2O$) and Ni^{2+} (from $Ni(NH_3)_6^{2+}$ to $Ni(NH_3)_6^{2+}{\cdot}12H_2O$) only results in an increase in $1000\ln{}^{15}\beta$ value for less than +1‰ at 25 °C, suggesting that the solvent effect is insignificant on metal-ammine complexes either.

Relative to $NH_{3(aqueous)}$, most metal-ammine complexes are more enriched in ^{15}N (Fig. 3B), which is in general consistent with that the metal-N bond in the complexes is stronger than the N-H bond in $NH_{3(aqueous)}$. However, the varying magnitudes of ^{15}N enrichment in the metal-ammine complexes relative to $NH_{3(aqueous)}$ suggest that more factors can affect the nitrogen isotope fractionations in the metal-ammine complexes. For example, compared with $NH_{3(aqueous)}$, $Zn(NH_3)_6^{2+}$ has slightly higher $^{15}\beta$ values and $Cd(NH_3)_6^{2+}$ has even slightly lower $^{15}\beta$ values (Table 5; Fig. 3B). Even taking into account a small increase from the solvent effect (<+1‰), nitrogen isotope fractionations between $Zn(NH_3)_6^{2+}$ or $Cd(NH_3)_6^{2+}$ and $NH_{3(aqueous)}$ are very small (<+2‰ at 0 °C). In contrast, the ammine complexes of Cu^+, Au^+, and Pt^+ have much higher $^{15}\beta$ values than $NH_{3(aqueous)}$. One speculation is that coordination of NH_3 in the metal-ammine complex may play an important role in determining the nitrogen isotope fractionations. As a fact, the $^{15}\beta$ values of metal-ammine complexes show an increasing trend following the decrease of coordination number from 6 (for Cd^{2+}, Zn^{2+}, Co^{2+}, Ni^{2+}, Co^{3+}), 4 (for Cd^{2+} and Cu^{2+}), to 2 (for Ag^+, Cu^+, Au^+, Pt^+) (see Fig. 3). The effect of NH_3 coordination can even overrule the valence effect, which is indicated by the inversed order in isotopic enrichment between $Cu(NH_3)_2^+$ and $Cu(NH_3)_4^{2+}$.

4.2. Comparison with literature data

Our calculated $^{15}\beta$ values for $NH_{3(gaseous)}$ are very close to those previous calculation results. For example, the calculations by Liu et al. (2010) using a similar method but a larger basis set gave a $^{15}\beta_{NH3(gaseous)}$ value of 1.0685 (vs. 1.0687 in this study) at 25 °C. In a recent study, Walters et al. (2019) also calculated the $^{15}\beta$ values for both gaseous and aqueous NH_3 and NH_4^+ in a temperature range of 250–350 K by the HF/6-31G(d) and B3LYP/6-31G(d) levels of theory and recommended to use the HF/6-31G(d) results. Therefore, in the discussions below, all data of Walters et al. (2019) refer to the HF/6-31G(d) results. Our calculation results agree relatively well with their results for $NH_{3(gaseous)}$ ($^{15}\beta$ value at 25 °C: 1.0687 in this study vs 1.0700 in Walters et al., 2019) and $NH_{4(gaseous)}^+$ ($^{15}\beta$ value at 25 °C: 1.1031 in this study vs 1.1049 in Walters et al., 2019) (Fig. 4B). However, our calculation results show a larger discrepancy to their results for $NH_{3(aqueous)}$ ($^{15}\beta$ value at 25 °C: 1.0776 in this study vs 1.0743 in Walters et al., 2019) and $NH_{4(aqueous)}^+$ ($^{15}\beta$ value at 25 °C: 1.1035 in this study vs 1.1073 in Walters et al., 2019). This discrepancy could be caused by two factors. First, it is noticed that, in the optimized geometry of Walters et al. (2019) for $NH_{3(aqueous)}$, the NH_3 molecule located at the edge of a water cluster, implying that this aqueous NH_3 model does not simulate a fully hydrated environment. Second, the calculations in Walters et al. (2019) only sampled one configuration for each explicit solvent model. However, previous studies have observed local configuration uncertainties caused by explicit solvent molecules and urged to sample multiple configurations (e.g., Table 3) to produce more accurate results (e.g., Zhang and Liu, 2014; He and Liu, 2015; Gao et al., 2018).

Nitrogen isotope fractionations between N_2 and NH_4^+ or NH_3 have been mostly investigated by theoretical calculations because it is difficult to reach isotope equilibrium between N_2 and NH_4^+ or NH_3 at experimental conditions (Li et al., 2009). Compared with previous theoretical calculations based on measured vibration frequencies (Urey, 1947; Scalan, 1958; Hanschmann, 1981; Petts et al., 2015), our results are closer to those of Scalan (1958) (see Fig. 4A).

Nitrogen isotope fractionations between NH_4^+ and $NH_{3(gaseous)}$ have been intensively studied by both theoretical calculations and experimental studies. The data are compiled in Fig. 4B. Our new results are broadly consistent with the results for a temperature range of 250–350 K by Walters et al. (2019). Compared with the diverse results in previous calculations based on measured vibration frequencies (Urey, 1947; Scalan, 1958; Hanschmann, 1981; Petts et al., 2015), our results fall between the results of Urey (1947) and Scalan (1958) at low temperature range (0–200 °C) but converge to those of Scalan (1958) and Hanschmann (1981) at temperatures higher than 200 °C (Fig. 4B). Among all these theoretical calculations, the results from Petts et al. (2015) are significantly lower than the others. This difference is mainly attributed to the large anharmonic effect from the calculations by Petts et al. (2015), which is however not observed in our calculations. Experimental determinations of nitrogen isotope fractionation between NH_4^+ and $NH_{3(gaseous)}$ were mostly carried out at low temperatures. The data of Thode et al. (1945), Kirshenbaum et al. (1947) and Heaton et al. (1997) are close to our calculation results (Fig. 4B), whereas the data of Urey and Aten (1936), Savard et al. (2017), Kawashima and Ono (2019) diverge from the theoretical predictions. This deviation may be attributed to two factors: (1) the equilibrium isotope fractionation could have not been achieved in those experiments; (2) some of the experiments were measured on solid ammonium salt, in which an additional isotope fractionation between solid NH_4^+ and gaseous NH_4^+ may exist (Ishimori, 1960b).

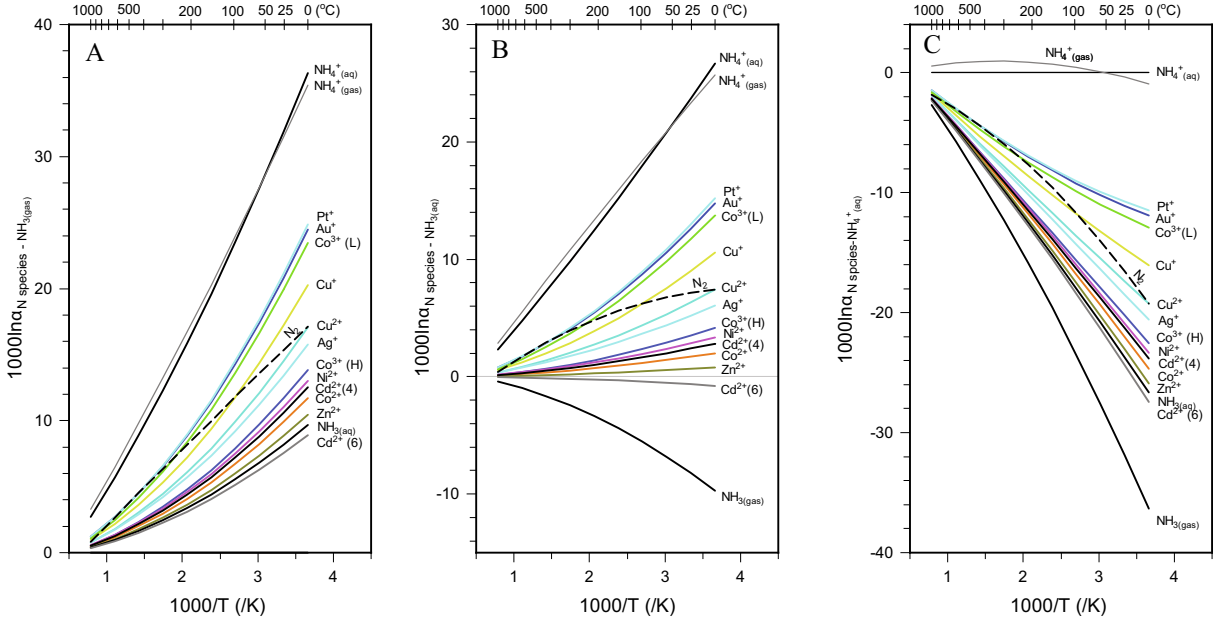

Fig. 3. Equilibrium nitrogen isotope fractionations of different nitrogen-bearing species relative to gaseous NH_3 (A), aqueous NH_3 (B), and aqueous ammonium (C). The letter "L" and "H" after Co^{3+} denote the low-spin state and the high-spin state, respectively. The number "4" and "6" after Cd^{2+} denote the coordination number of NH_3.

Nitrogen isotope fractionations between NH_4^+ and $NH_{3(aqueous)}$ are relatively less studied. The solvent effect, which is strong for NH_3 hydration but negligible for NH_4^+ hydration, results in diminished isotope fractionation between the NH_4^+ – $NH_{3(aqueous)}$ pair relative to the NH_4^+ – $NH_{3(gaseous)}$ pair. This has been demonstrated by our calculation as well as those by Walters et al. (2019). However, our calculations yielded much smaller magnitudes of nitrogen isotope fractionations between NH_4^+ and $NH_{3(aqueous)}$ (Fig. 4C) than those of Walters et al. (2019), likely because the calculations in Walters et al. (2019) only incorporated a partial solvent effect, which can be inferred by the configuration of their hydrated NH_3. Our results fit well with the experimental results of Urey and Aten (1936), Thode et al. (1945), and Ishimori (1960a), but are slightly lower than the result of Kirshenbaum et al. (1947) and slightly higher than the result of Hermes et al. (1985). One striking phenomenon on Fig. 4C is that the experimental results by Li et al. (2012) are much higher than the theoretical predictions, which will be explored in detail in Section 5.1.

For the $NH_{3(aqueous)}$ – $NH_{3(gaseous)}$ pair (Fig. 4D), our calculations considering a full hydration effect yielded larger nitrogen isotope fractionations than those of Walters et al. (2019). The relatively few experimental estimates (e.g., Wahl et al., 1935; Urey and Aten, 1936; Thode et al., 1945; Kirshenbaum et al., 1947; Deng et al., 2018) mostly fall between the line from this study and the one from Walters et al. (2019). The difference between our results and the experimental results may be attributed to the kinetic isotope effect associated with the movement of NH_3 gas (e.g., Deng et al., 2018), which could have interfered the quantification of the equilibrium isotope fractionations in laboratory experiments.

The study of nitrogen isotope fractionation involving metal-ammine complexes is very few in our knowledge. By ion-exchange experiments using cation exchange resins, Ishimori (1960a) investigated the equilibrium isotope fractionation factors during the single-stage separation of NH_3 from ammine complexes of Ni^{2+}, Cu^{2+}, Zn^{2+}, Cd^{2+}, and Ag^{2+} in 30 °C aqueous solutions, which yielded +7.6‰ between $Ni(NH_3)_n^{2+}$ and NH_3, +11.6‰ between $Cu(NH_3)_4^{2+}$ and NH_3, +11.5‰ between $Zn(NH_3)_4^{2+}$ and NH_3, +10.2‰ between $Cd(NH_3)_4^{2+}$ and NH_3, and +9.2‰ between $Ag(NH_3)_2^{2+}$ and NH_3. Using similar experiments at 30 °C, Gupta and Sarpal (1967) obtained the equilibrium isotope fractionation factors of +6.2‰, +7.9‰, and +10.0‰ between Ni^{2+}-ammine complexes and NH_3 in aqueous solutions during the single-stage separation of NH_3 from $Ni(NH_3)_4^{2+}$, $Ni(NH_3)_5^{2+}$, and $Ni(NH_3)_6^{2+}$, respectively. These experimental and theoretical data are significantly higher than our calculated data between these metal-ammine complexes and $NH_{3(aqueous)}$ (e.g., +2.8‰ for $Ni(NH_3)_6^{2+}$, +2.3‰ for $Cd(NH_3)_4^{2+}$, +6.2‰ for $Cu(NH_3)_4^{2+}$, +0.6‰ for $Zn(NH_3)_6^{2+}$, +5.1‰ for $Ag(NH_3)_2^{+}$, at 30 °C), but mostly lower than those between metal-ammine complexes and $NH_{3(gaseous)}$ (e.g., +10.8‰ for $Ni(NH_3)_6^{2+}$, +10.3‰ for $Cd(NH_3)_4^{2+}$, +14.2‰ for $Cu(NH_3)_4^{2+}$, +8.6‰ for $Zn(NH_3)_6^{2+}$, +13.1‰ for $Ag(NH_3)_2^{+}$, at 30 °C). Because these experimental studies (Ishimori, 1960a; Gupta and Sarpal, 1967) did not describe the detailed controlling conditions in their experiments, in particular, whether other nitrogen species (e.g., NH_4^+)

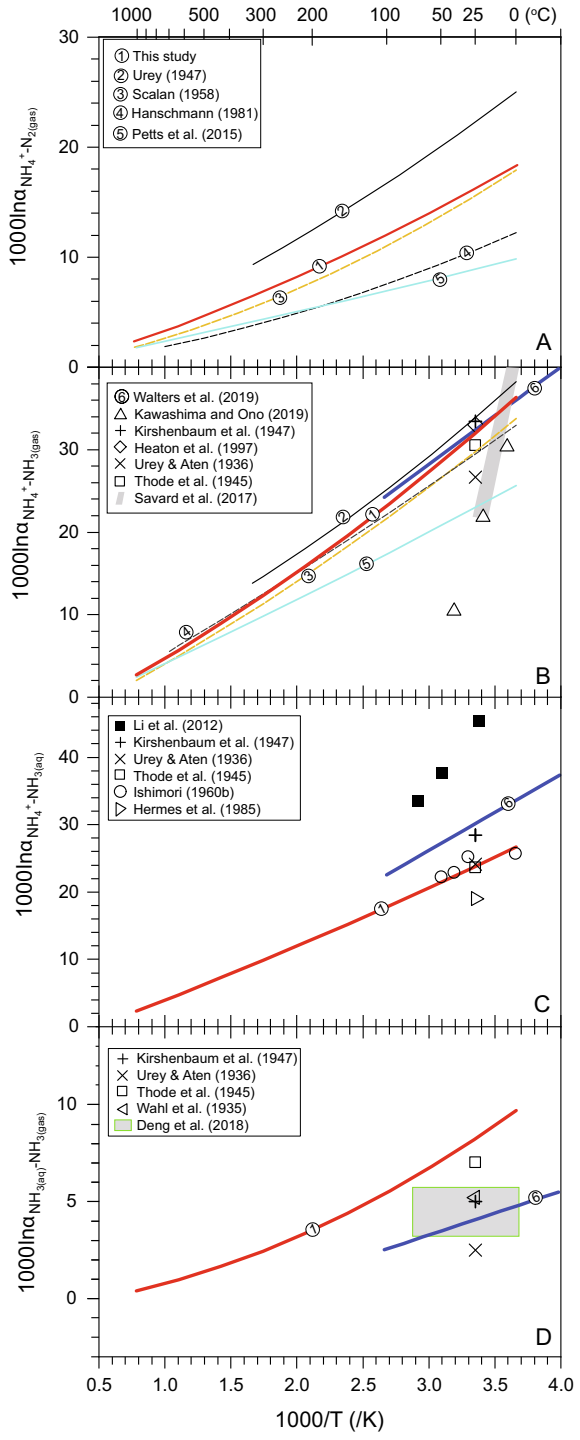

Fig. 4. Comparison of nitrogen isotope fractionation factors between our data and previous theoretical calculations and experimental results. The line numers in B, C and D are the same to those in A. See text for discussion.

coexisted in the solution or whether any NH_3 degassing was involved, it is difficult to assess the exact cause of the discrepancy between our calculation results and these experimental results. In a theoretical calculation based on vibrational frequency data, Jeevanandam and Gupta (1968) obtained the isotope fractionation factors (relative to NH_3) at 25 °C to be ~ +27‰ for $Co(NH_3)_6^{3+}$, ~ +15‰ for $Ni(NH_3)_6^{2+}$, and ~ +11‰ for $Co(NH_3)_6^{2+}$, which are slightly higher than our calculated results between these complexes and gaseous NH_3, i.e., +11.8‰ and + 20.0‰ for $Co(NH_3)_6^{3+}$ at high-spin state and low-spin state, repsectively, +11.1‰ for $Ni(NH_3)_6^{2+}$, and ~ +10.0‰ for $Co(NH_3)_6^{2+}$.

5. APPLICATIONS

5.1. Complicated isotopic effect during NH3 degassing

NH_3 degassing may occur in alkaline fluids in a variety of geological settings (see discussion in Li et al., 2012; Deng et al., 2018). Li et al. (2012) carried out laboratory experiments to simulate NH_3 degassing in the field at a temperature range from 2 °C to 70 °C. The experiments were started by adding inadequate hydroxyl to partially dissociate NH_4^+ in a solution to drive NH_3 degassing, i.e., the processes described by Eq. (1). The nitrogen isotopic compositions of the remaining NH_4^+ after complete degassing of NH_3 produced by partial dissociation of NH_4^+ at various extents displayed a pattern close to batch equilibrium model rather than a Rayleigh model, which made the observed large isotopic effect (from +33.5‰ at 70 °C to +45.5‰ at 23 °C) be interpreted as a result mainly from equilibrium isotope fractionations between NH_4^+ and $NH_{3(aqueous)}$, whereas the possible effect from NH_3 degassing was not fully assessed due to the lack of data (Li et al., 2012). Our calculations yielded significantly smaller nitrogen isotope fractionations between NH_4^+ and $NH_{3(aqueous)}$ (Fig. 4C) than the experimental results by Li et al. (2012). Recently, experimental investigations on the $NH_{3(aqueous)}$ – NH_3 system by Deng et al. (2018) revealed that NH_3 degassing could have a significant kinetic nitrogen isotope effect. To assess the possible influence of this kinetic isotope effect on the experimental results in Li et al. (2012), we carried out numeric modeling of those isotopic results using the equilibrium isotope fractionation factors between NH_4^+ and $NH_{3(aqueous)}$ in this study and the kinetic isotope effect between $NH_{3(aqueous)}$ and $NH_{3(gaseous)}$ determined by Deng et al. (2018).

Following the methods from previous studies (e.g., Rees, 1973; Dauphas and Rouxel, 2006), a two-step reaction model was applied to characterize the nitrogen isotope fractionation involving an intermediate species. The nitrogen isotope transfer in the reaction network can be described by the equations below.

$$\begin{aligned} &{}^{14}NH_4^+ + OH^- + (n-1)H_2O \overset{{}^{14}k_1}{\underset{{}^{14}k_2}{\rightleftharpoons}} {}^{14}NH_3 \cdot nH_2O \\ &\times \overset{{}^{14}k_3}{\rightarrow} {}^{14}NH_{3(gas)} + nH_2O \\ &{}^{15}NH_4^+ + OH^- + (n-1)H_2O \overset{{}^{15}k_1}{\underset{{}^{15}k_2}{\rightleftharpoons}} {}^{15}NH_3 \cdot nH_2O \\ &\times \overset{{}^{15}k_3}{\rightarrow} {}^{15}NH_{3(gas)} + nH_2O \end{aligned} \quad (6)$$

in which $^{14}k_1$, $^{15}k_1$, $^{14}k_2$, $^{15}k_2$, $^{14}k_3$, $^{15}k_3$ represent reaction rates of ^{14}N and ^{15}N in the reversible reaction between NH_4^+ and $NH_{3(aqueous)}$ (denoted by subscripts 1 and 2)

and the unidirectional reaction from $NH_{3(aqueous)}$ to $NH_{3(gaseous)}$ (denoted by subscript 3), respectively. Accordingly, the concentration of reactants and products at time t can be obtained by:

$$\frac{dn_{[\ ^{14}NH_4^+]}}{dt} = -\ ^{14}k_1\left[\ ^{14}NH_4^+\right]\cdot[HO^-] + \ ^{14}k_2\left[\ ^{14}NH_3\cdot nH_2O\right] \quad (7)$$

$$\frac{dn_{[\ ^{15}NH_4^+]}}{dt} = -\ ^{15}k_1\left[\ ^{15}NH_4^+\right]\cdot[HO^-] + \ ^{15}k_2\left[\ ^{15}NH_3\cdot nH_2O\right] \quad (8)$$

$$\frac{dn_{[\ ^{14}NH_3\cdot nH_2O]}}{dt} = \ ^{14}k_1\left[\ ^{14}NH_4^+\right]\cdot[HO^-] - \ ^{14}k_2\left[\ ^{14}NH_3\cdot nH_2O\right] - \ ^{14}k_3\left[\ ^{14}NH_3\cdot nH_2O\right] \quad (9)$$

$$\frac{dn_{[\ ^{15}NH_3\cdot nH_2O]}}{dt} = \ ^{15}k_1\left[\ ^{15}NH_4^+\right]\cdot[HO^-] - \ ^{15}k_2\left[\ ^{15}NH_3\cdot nH_2O\right] - \ ^{15}k_3\left[\ ^{15}NH_3\cdot nH_2O\right] \quad (10)$$

$$\frac{dn_{[\ ^{14}NH_3\cdot nH_2O]}}{dt} = \ ^{14}k_3\left[\ ^{14}NH_3\cdot nH_2O\right] \quad (11)$$

$$\frac{dn_{[\ ^{15}NH_3\cdot nH_2O]}}{dt} = \ ^{15}k_3\left[\ ^{15}NH_3\cdot nH_2O\right] \quad (12)$$

Finally, the ratio of the remaining NH_4^+ and $NH_{3(aqueous)}$ ($R_{remaining}$) at time t can be derived from:

$$R_{remaining} = \frac{\left[\ ^{15}NH_4^+\right] + \left[\ ^{15}NH_3\cdot nH_2O\right]}{\left[\ ^{14}NH_4^+\right] + \left[\ ^{14}NH_3\cdot nH_2O\right]} \quad (13)$$

The nitrogen isotope fractionations in these reactions can be described as:

$$\alpha_1 = \frac{^{15}k_1\cdot\ ^{14}k_2}{^{15}k_2\cdot\ ^{14}k_1} \quad (14)$$

$$\alpha_2 = \frac{^{15}k_3}{^{14}k_3} \quad (15)$$

where α_1 is the equilibrium nitrogen isotope fractionation factor, which has been calculated above; α_2 is the kinetic nitrogen isotope fractionation factor, which has been determined by Deng et al. (2018). In our numeric modeling, values were arbitrarily assigned to the unknowns $^{14}K_1$, $^{15}K_1$, and $^{14}K_2$ to best fit the experimental data.

When hydroxyl is added into an ammonium solution, the extent of the overall reaction is dependent on the initial $[OH^-]/[NH_4^+]$ ratio. As a combined effect of equilibrium isotope fractionation between the remaining NH_4^+ and $NH_{3(aqueous)}$ and kinetic isotope fractionation of NH_3 degassing from $NH_{3(aqueous)}$, the remaining NH_4^+ in the solution is progressively enriched in ^{15}N with the proceeding of the reaction until the produced $NH_{3(aqueous)}$ is consumed by NH_3 degassing. The magnitude of ^{15}N enrichment in the remaining NH_4^+ is a function of (1) temperature, which determines the magnitudes of the two involved isotope fractionations, and (2) the initial $[OH^-]/[NH_4^+]$ ratio, which determines the extents of the total reaction. The progressive ^{15}N enrichment patterns for reactions at room temperature, 50 °C and 70 °C, are illustrated in Fig. 5 for a variety of initial $[OH^-]/[NH_4^+]$ ratios. The results show that, when the initial $[OH^-]/[NH_4^+]$ ratio is large enough (e.g., ≥ 2) to drive complete conversion of NH_4^+ to $NH_{3(aqueous)}$, the ^{15}N enrichment in the remaining $NH_{3(aqueous)}$ along progressive NH_3 degassing is only controlled by the kinetic isotope fractionation from NH_3 degassing and follows the red curves in Fig. 5A-C. These scenarios resemble the laboratory experiments by Deng et al. (2018), and consistently, the data from Deng et al. (2018) fall closely to these curves. In contrast, when the initial $[OH^-]/[NH_4^+]$ ratio is small enough (e.g., ≤ 1) to only induce partial conversion of NH_4^+ to $NH_{3(aqueous)}$, the isotope evolution pattern of the remaining nitrogen in the solution (a mixture of NH_4^+ and $NH_{3(aqueous)}$ in this case) along progressive NH_3 degassing is controlled by both equilibrium and kinetic isotopic fractionations as well as the initial $[OH^-]/[NH_4^+]$ ratio. The progressive ^{15}N enrichments for a number of initial $[OH^-]/[NH_4^+]$ ratios are illustrated by the grey curves in Fig. 5. Interestingly, after complete degassing of NH_3 from the solution, the $\delta^{15}N$ of the remaining NH_4^+ from varying initial $[OH^-]/[NH_4^+]$ ratios, i.e., the data points at the ends of the grey curves on Fig. 5, form the blue curves which show very small curvatures that mimic batch equilibration lines as initially thought in Li et al. (2012). When plotted on Fig. 5, the experimental data of Li et al. (2012) align closely along the blue lines. Therefore, the large isotope fractionations observed in the experiments by Li et al. (2012) more likely reflect the overall isotope effect combining the equilibrium isotope fractionation during the conversion of NH_4^+ to $NH_{3(aqueous)}$ (this study) and the kinetic isotope effect of NH_3 degassing (Deng et al., 2018). Nevertheless, the experiments in Li et al. (2012) represent an open-system scenario that is more likely to occur in the field, and thus can contribute to interpret the field data in a first order. More accurate data modeling and interpretation should follow the quantitative modeling described here (Eqs. (7)–(15); Fig. 5).

5.2. Metal-ammine remobilization in hydrothermal system?

Busigny et al. (2011) observed a linear relationship between Cu concentration and $\delta^{15}N$ values in metagabbros from the western Alps. To explain this correlation, the authors proposed that Cu in the protoliths of the metagabbros was hydrothermal leached and remobilized by fluid in which ammonia is complexed with Cu. However, because the nitrogen isotope fractionation factors between Cu-ammine complex (the species in the fluid) and ammonium (the species in the (meta-)mafic rocks; Busigny et al., 2005, 2011; Li et al., 2007, 2014) were not available at that time, Busigny et al. (2011) modeled their data using the nitrogen isotope fractionation factors between NH_4^+ and NH_3 from Scalan (1958), which are now demonstrated to be very different from those between NH_4^+ and copper-ammine complex (see Fig. 3). Our new data provide an unprecedently available opportunity to revisit this hypothesis.

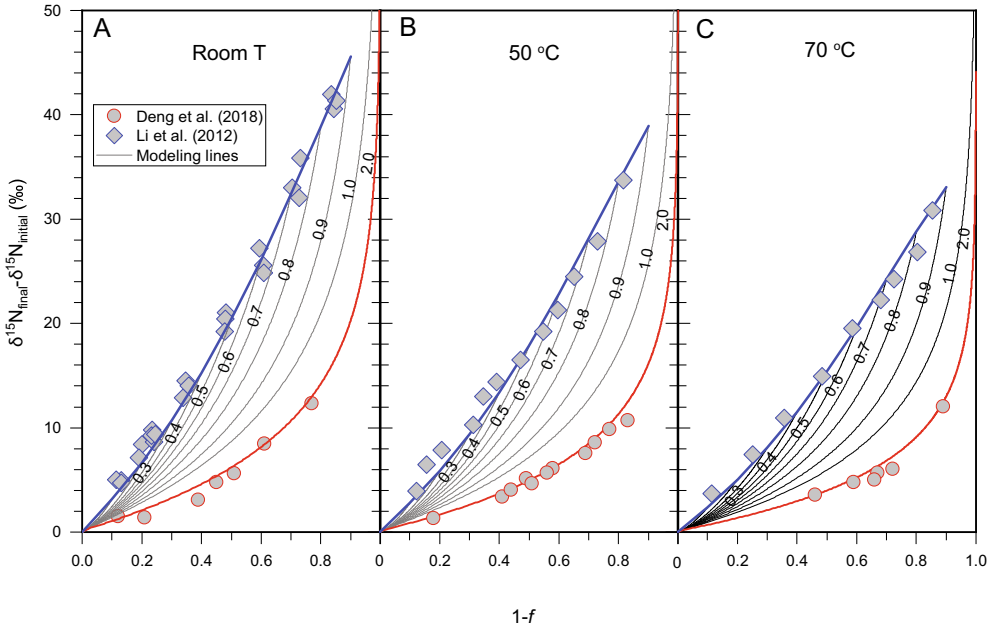

Fig. 5. Diagram showing the progressive ^{15}N enrichment in the remaining nitrogen in a solution along progressive degassing of NH_3 as a result of partial dissociation of NH_4^+. Number on individual line refers to the initial ratio of $[OH^-]/[NH_4^+]$ in the solution, which determines the fraction of NH_4^+ that can be dissocaited and eventually degassed. The end point on each curve represents the isotopic composition of the final remaining NH_4^+ in the solution (if there is any) after complete NH_3 degassing. The blue lines linking these end points fit well with the experimental data of Li et al. (2012). The red lines represent the case of complete dissociation of NH_4^+, which fit well with the experimental results of Deng et al. (2018). See text for discussion.

In our modeling (see Fig. 6), the valence of copper cation is considered to be either I or II. The coordination number for copper cation is strongly dependent on solution environments. Cu(II) can have coordination numbers of 4, 5 and 6, among which $Cu(NH_3)_4^{2+}$ is the most thermodynamically stable species; whereas Cu (I) can have coordination numbers of 2, 3 and 4, among which the most thermodynamically stable species has been suggested to be $Cu(NH_3)_2^+$ (Pavelka and Burda, 2005). Using the calculated nitrogen isotope fractionations of these two species relative to ammonium (Table 6; Fig. 3C), we modeled the meta-gabbro data from Busigny et al. (2011) by a batch model. Rayleigh distillation model is not employed here because it is apparently inconsistent with the observed linear relationship between Cu concentration and $\delta^{15}N$ of the low-strain meta-gabbros samples.

Fig. 6 illustrates our modeling results. It shows that the relationship between nitrogen concentrations and $\delta^{15}N$ values can be easily explained by a leaching model (as well as a mixing model or a batch devolatilization model), but requires a large temperature range, e.g., 250–650 °C if in form of $Cu(NH_3)_2^+$ or 300–700 °C if in form of $Cu(NH_3)_4^{2+}$ (Fig. 6A). Applying the same temperature ranges, the Cu concentration and $\delta^{15}N$ data should fall in the triangular area labeled by $Cu(NH_3)_2^+$ or $Cu(NH_3)_4^{2+}$ in Fig. 6B, which however cannot explain the observed Cu data because of the low efficiency of NH_3 in mobilizing Cu in these two forms, i.e., 2:1 and 4:1, respectively (Fig. 6B). If copper mobilization was indeed coupled with NH_3 in those samples, it had to be in a copper complex species containing only one NH_3 (Fig. 6B) in order to efficiently leach out > 90% of the Cu as observed in some samples (Fig. 6B). In this case, the Cu concentration – $\delta^{15}N$ relationship can be explained by a batch model (the triangular area labeled by $Cu(NH_3)^{+/2+}$ in Fig. 6B) with $\ln\alpha_{NH_4^+-Cu(NH_3)^{+/2+}}$ values of +7.5‰ to + 10.1‰. Even applying the isotope fractionations of $Cu(NH_3)_4^{2+}$ or $Cu(NH_3)_2^+$, which have larger coordination numbers than the expected species of $Cu(NH_3)^{2+}$ or $Cu(NH_3)^+$, respectively, these large isotope fractionations correspond to a small temperature range of 200–320 °C for Cu^{2+} or 150–270 °C for Cu^+, both are significantly lower than the large and high temperature ranges to explain the N concentration – $\delta^{15}N$ relationship (Fig. 6A). The real isotope fractionations between NH_4^+ and $Cu(NH_3)^{+/2+}$ would be smaller than these between NH_4^+ and $Cu(NH_3)_4^{2+}$ or between NH_4^+ and $Cu(NH_3)_2^+$ given that ^{15}N is expected to be more enriched in species with smaller coordination numbers. Consequently, it requires even lower temperature range to explain the data. This self-inconsistency between the temperature ranges yielded from the N content-$\delta^{15}N$ relationship (Fig. 6A) and from the Cu content-$\delta^{15}N$ relationship (Fig. 6B) implies that the observed nitrogen signature of the meta-gabbros (Busigny et al., 2011) might not be controlled by leaching during seafloor hydrothermal alteration, or at least have been overprinted by other geochemical processes.

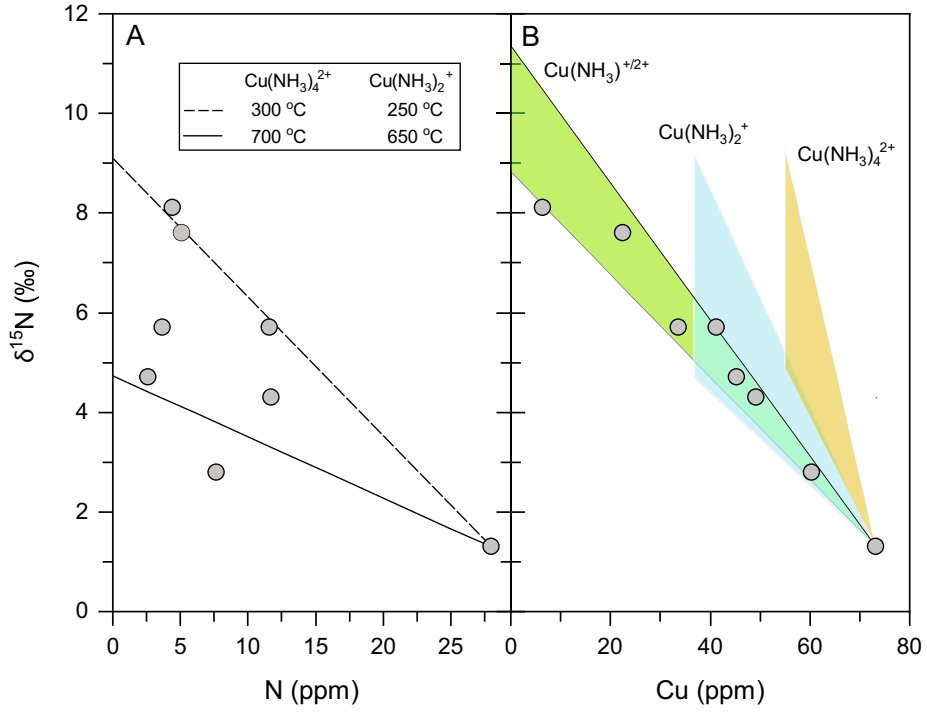

Fig. 6. Modeling of Cu and N contents versus nitrogen isotope compositions of meta-gabbros from the western Alps following the model of a coupled leaching of Cu and NH_3 by Busigny et al. (2011). See text for discussion.

6. CONCLUSION

Theoretical calculations of equilibrium nitrogen isotope fractionation factors between gaseous and aqueous ammonium, ammonia, N_2 and metal-ammine complexes indicate that ^{15}N is enriched following the order of $NH_4^+ > N_2 - > NH_{3(aqueous)} > NH_{3(gaseous)}$, with all but one metal-ammine complexes lying between NH_4^+ and $NH_{3(aqueous)}$. Our calculation suggests anharmonic effect is not significant on the isotope fractionation between NH_4^+ and NH_3. In the metal-ammine complexes, coordination number may play an important role in controlling the isotope fractionations. Our new calculation results verify that nitrogen isotope behavior in a natural system involving multiple nitrogen species may be very complicated. The propagation of isotope fractionations along a reaction network may result in a much larger isotopic effect than expected.

Declaration of Competing Interest

The authors declare that they have no known competing financial interests or personal relationships that could have appeared to influence the work reported in this paper.

ACKNOWLEDGEMENTS

This study is supported by the NSERC-Discovery Grant to LL, the China Postdoctoral Science Foundation [2019M660811] to YH, and Chinese NSF project [41530210] to YL. We thank Y. Zhang for performing the anharmonic tests and valuable discussions. The paper has been greatly improved by constructive comments from Associate Editor Dr. M. Blanchard, Dr. S. Mikhail, and two anonymous reviewers.

APPENDIX A. SUPPLEMENTARY MATERIAL

Supplementary data to this article can be found online at https://doi.org/10.1016/j.gca.2020.12.010.

REFERENCES

Barnet M., Craven B., Freeman H., Kime N. and Ibers J. A. (1966) The Co–N bond lengths in Co II and Co III hexammines. *Chem. Commun. (London)*, 307–308.

Bebout G. E. and Fogel M. L. (1992) Nitrogen-isotope compositions of metasedimentary rocks in the Catalina Schist, California: implications for metamorphic devolatilization history. *Geochim. Cosmochim. Acta* **56**, 2839–2849.

Bebout G. E., Cooper D. C., Bradley A. D. and Sadofsky S. J. (1999) Nitrogen-isotope record of fluid-rock interactions in the Skiddaw Aureole and granite, English Lake District. *Amer. Mineral.* **84**, 1495–1505.

Bebout G. E., Lazzeri K. E. and Geiger C. A. (2016) Pathways for nitrogen cycling in Earth's crust and upper mantle: A review and new results for microporous beryl and cordierite. *Amer. Mineral.* **101**, 7–24.

Becke A. D. (1993) Density-functional thermochemistry. III. The role of exact exchange. *J. Chem. Phys.* **98**, 5648–5652.

Bigeleisen J. and Mayer M. G. (1947) Calculation of equilibrium constants for isotopic exchange reactions. *J. Chem. Phys.* **15**, 261–267.

Blanchard M., Balan E. and Schauble E. A. (2017) Equilibrium fractionation of non-traditional isotopes: A molecular modeling perspective. *Rev. Mineral. Geochem.* **82**, 27–63.

Brandes J. A., Boctor N. Z., Cody G. D., Cooper B. A. and Hazen R. M. (1998) Abiotic nitrogen reduction on the early Earth. *Nature* **395**, 365–367.

Busigny V. and Bebout G. E. (2013) Nitrogen in the silicate Earth: Speciation and isotopic behavior during mineral–fluid interactions. *Elements* **9**, 353–358.

Busigny V., Laverne C. and Bonifacie M. (2005) Nitrogen content and isotopic composition of oceanic crust at a superfast spreading ridge: a profile in altered basalts from ODP Site 1256, Leg 206. *Geochem. Geophys. Geosyst.* **6**, Q12O01.

Busigny V., Cartigny P. and Philippot P. (2011) Nitrogen isotopes in ophiolitic metagabbros: A re-evaluation of modern nitrogen fluxes in subduction zones and implication for the early Earth atmosphere. *Geochim. Cosmoch. Acta* **75**, 7502–7521.

Busigny V., Cartigny P., Philippot P., Ader M. and Javoy M. (2003) Massive recycling of nitrogen and other fluid-mobile elements (K, Rb, Cs, H) in a cold slab environment: evidence from HP to UHP oceanic metasediments of the Schistes Lustrés nappe (western Alps, Europe). *Earth Planet. Sci. Lett.* **215**, 27–42.

Cao X. and Liu Y. (2012) Theoretical estimation of the equilibrium distribution of clumped isotopes in nature. *Geochim. Cosmoch. Acta* **77**, 292–303.

Casanova D. and Head-Gordon M. (2009) Restricted active space spin-flip configuration interaction approach: theory, implementation and examples. *Phys. Chem. Chem. Phys.* **11**, 9779–9790.

Chen F. and Davidson E. R. (2001) Electronic, structural, and hyperfine interaction investigations on rydberg molecules: NH_4, OH_3, and FH_2. *J. Phys. Chem. A* **105**, 10915–10921.

Chu T.-Y.-J., Steiner G. R. and McEntyre C. L. (1978) Removal of complex copper-ammonia ions from aqueous wastes with fly ash. *J. (Water Pollution Control Federation)* **50**, 2157–2174.

Dauphas N. and Rouxel O. (2006) Mass spectrometry and natural variations of iron isotopes. *Mass Spectrom. Rev.* **25**, 515–550.

Dauphas N. and Schauble E. A. (2016) Mass fractionation laws, mass-independent effects, and isotopic anomalies. *Ann. Rev. Earth. Planet. Sci.* **44**, 709–783.

Deng Y., Li Y. and Li L. (2018) Experimental investigation of nitrogen isotopic effects associated with ammonia degassing at 0–70 °C. *Geochim. Cosmochim. Acta* **226**, 182–191.

Duit W., Jansen J. B. H., Van Breemen A. and Bos A. (1986) Ammonium micas in metamorphic rocks as exemplified by Dome de l'Agout (France). *Amer. J. Sci.* **286**, 702–732.

Eldridge D., Guo W. and Farquhar J. (2016) Theoretical estimates of equilibrium sulfur isotope effects in aqueous sulfur systems: highlighting the role of isomers in the sulfite and sulfoxylate systems. *Geochim. Cosmochim. Acta* **195**, 171–200.

Eßmann R. (1995) Influence of coordination on N-H··· X– hydrogen bonds. Part 1. [Zn (NH3)4] Br 2 and [Zn (NH3)4]I2. *J. Molecul. Struct.* **356**, 201–206.

Fatmi M. Q., Hofer T. S., Randolf B. R. and Rode B. M. (2006) Structure and dynamics of the $[Zn\ (NH_3)(H_2O)_5]^{2+}$ complex in aqueous solution obtained by an ab initio QM/MM molecular dynamics study. *Phys. Chem. Chem. Phys.* **8**, 1675–1681.

Fatmi M. Q., Hofer T. S. and Rode B. M. (2010) The stability of $[Zn(NH_3)_4]^{2+}$ in water: a quantum mechanical/molecular mechanical molecular dynamics study. *Phys. Chem. Chem. Phys.* **12**, 9713–9718.

Fox B. S., Beyer M. K. and Bondybey V. E. (2002) Coordination chemistry of silver cations. *J. Am. Chem. Soc.* **124**, 13613–13623.

Frisch M. J., Pople J. A. and Binkley J. S. (1984) Self-consistent molecular orbital methods 25. Supplementary functions for Gaussian basis sets. *J. Chem. Phys.* **80**, 3265–3269.

Frisch, M.J., Trucks, G.W., Schlegel, H.B., Scuseria, G.E., Robb, M.A., Cheeseman, J.R., Scalmani, G., Barone, V., Petersson, G.A., Nakatsuji, H., Li, X., Caricato, M., Marenich, A.V., Bloino, J., Janesko, B.G., Gomperts, R., Mennucci, B., Hratchian, H.P., Ortiz, J.V., Izmaylov, A.F., Sonnenberg, J. L., Williams, Ding, F., Lipparini, F., Egidi, F., Goings, J., Peng, B., Petrone, A., Henderson, T., Ranasinghe, D., Zakrzewski, V.G., Gao, J., Rega, N., Zheng, G., Liang, W., Hada, M., Ehara, M., Toyota, K., Fukuda, R., Hasegawa, J., Ishida, M., Nakajima, T., Honda, Y., Kitao, O., Nakai, H., Vreven, T., Throssell, K., Montgomery Jr., J.A., Peralta, J.E., Ogliaro, F., Bearpark, M.J., Heyd, J.J., Brothers, E.N., Kudin, K.N., Staroverov, V.N., Keith, T.A., Kobayashi, R., Normand, J., Raghavachari, K., Rendell, A.P., Burant, J.C., Iyengar, S.S., Tomasi, J., Cossi, M., Millam, J.M., Klene, M., Adamo, C., Cammi, R., Ochterski, J.W., Martin, R.L., Morokuma, K., Farkas, O., Foresman, J.B. and Fox, D.J. (2016) Gaussian 16 Rev. B.01. 2016.

Gao C., Cao X., Liu Q., Yang Y., Zhang S., He Y., Tang M. and Liu Y. (2018) Theoretical calculation of equilibrium Mg isotope fractionations between minerals and aqueous solutions. *Chem. Geol.* **488**, 62–75.

Geddes A. L. and Bottger G. L. (1969) Infrared spectra of silver-ammine complexes. *Inorg. Chem.* **8**, 802–807.

Gupta A. R. and Sarpal S. (1967) Nitrogen isotope effects in nickel-ammonia complex and ammonia system. *J. Phys. Chem.* **71**, 500–508.

Halama R., Bebout G. E., John T. and Schenk V. (2010) Nitrogen recycling in subducted oceanic lithosphere: The record in high- and ultrahigh-pressure metabasaltic rocks. *Geochim. Cosmochim. Acta* **74**, 1636–1652.

Halama R., Bebout G. E., John T. and Scambelluri M. (2014) Nitrogen recycling in subducted mantle rocks and implications for the global nitrogen cycle. *Inter. J. Earth Sci.* **103**, 2081–2099.

Halama R., Bebout G. E., Marschall H. R. and John T. (2017) Fluid-induced breakdown of white mica controls nitrogen transfer during fluid–rock interaction in subduction zones. *Inter. Geol. Rev.* **59**, 702–720.

Han K., Hoover M. and Fuerstenau D. (1974) Ammonia-ammonium leaching of deep-sea manganese nodules. *Inter. J. Mineral Process.* **1**, 215–230.

Hanschmann G. (1981) Berechnung von Isotopieeffekten auf quantenchemischer Grundlage am Beispiel stick-stoffhaltiger Moleküle. *ZFI-Mitt.* **41**, 19–39.

Hathaway B. and Tomlinson A. (1970) Copper (II) ammonia complexes. *Coord. Chem. Rev.* **5**, 1–43.

Hay P. J. and Wadt W. R. (1985) Ab initio effective core potentials for molecular calculations. Potentials for K to Au including the outermost core orbitals. *J. Chem. Phys.* **82**, 299–310.

Haynes W. M. (2014) *CRC Handbook of Chemistry and Physics*. CRC Press.

He H. and Liu Y. (2015) Silicon isotope fractionation during the precipitation of quartz and the adsorption of H4SiO4 (aq) on Fe (III)-oxyhydroxide surfaces. *Chin. J. Geochem.* **34**, 459–468.

Hermes J. D., Weiss P. M. and Cleland W. W. (1985) Use of nitrogen-15 and deuterium isotope effects to determine the chemical mechanism of Phenylalanine ammonia-lyaset. *Biochemistry* **25**, 2959–2967.

Heaton T. H. E., Spiro B. and Robertson S. M. C. (1997) Potential canopy influences on the isotopic composition of nitrogen and sulphur in atmospheric deposition. *Oecologia* **109**, 600–607.

Hill P. S. and Schauble E. A. (2008) Modeling the effects of bond environment on equilibrium iron isotope fractionation in ferric aquo-chloro complexes. *Geochim. Cosmochim. Acta* **72**, 1939–1958.

Holloway J. M., Nordstrom D. K., Bohlke J., McCleskey R. B. and Ball J. W. (2011) Ammonium in thermal waters of Yellowstone National Park: processes affecting speciation and isotope fractionation. *Geochim. Cosmochim. Acta* **75**, 4611–4636.

Holm N. G., Dumont M., Ivarsson M. and Konn C. (2006) Alkaline fluid circulation in ultramafic rocks and formation of nucleotide constituents: a hypothesis. *Geochem. Trans.* **7**, 7. https://doi.org/10.1186/1467-4866-7-7.

Honma H. and Itihara Y. (1981) Distribution of ammonium in minerals of metamorphic and granitic rocks. *Geochim. Cosmochim. Acta* **45**, 983–988.

Katsiapi A., Tsakiridis P. E., Oustadakis P. and Agatzini-Leonardou S. (2010) Cobalt recovery from mixed Co-Mn hydroxide precipitates by ammonia-ammonium carbonate leaching. *Miner. Eng.* **23**, 643–651.

Irving H. and Williams R. J. P. (1953) 637. The stability of transition-metal complexes. *J. Chem. Soc. (Resumed)*, 3192–3210.

Ishimori T. (1960a) Nitrogen isotopic equilibria between ammonia and metal-ammine complex ions in aqueous solution. *Bullet. Chem. Soc. Japan* **33**, 520–523.

Ishimori T. (1960b) The nitrogen isotopic equilibrium between ammonia and ammonium ion. *Bullet. Chem. Soc. Japan* **33**, 516–519.

Jeevanandam M. and Gupta A. R. (1968) Nitrogen isotope effect in transition metal hexaammine complex-ammonia systems: A theoretical consideration. *J. Phys. Chem.* **73**, 2472–2477.

Juhász M., Takahashi S., Arulmozhiraja S. and Fujii T. (2012) Bond energies (Pt-NH3, Pt-Cl) and proton affinity of cisplatin: A density functional theory approach. *J. Struct. Chem.* **53**, 436–442.

Kawashima H. and Ono S. (2019) Nitrogen isotope fractionation from ammonia gas to ammonium in particulate ammonium chloride. *Environ. Sci. Technol.* **53**, 10629–10635.

Kim K. S., Lee S., Mhin B. J., Cho S. J. and Kim J. (1993) Structures and energetics of $Zn(NH_3)^{2+}$ n (n= 4–6). Coordination number of Zn^{2+} by ammine. *Chem. Phys. Lett.* **216**, 309–312.

Kirshenbaum I., Smith J. S., Crowell T., Graff J. and McKee R. (1947) Separation of the nitrogen isotopes by the exchange reaction between ammonia and solutions of ammonium nitrate. *J. Chem. Phys.* **15**, 440–446.

Klots C. E. and Benson B. B. (1963) Isotope effect in the solution of oxygen and nitrogen in distilled water. *J. Chem. Phys.* **38**, 890–892.

Kryachko E. S. and Remacle F. (2007) The gold-ammonia bonding patterns of neutral and charged complexes Aum0±1–(NH3)n. I. Bonding and charge alternation. *J. Chem. Phys.* **127** 194305.

Lee C., Yang W. and Parr R. G. (1988) Development of the Colle-Salvetti correlation-energy formula into a functional of the electron density. *Phys. Rev. B.* **37**, 785–789.

Li Y. and Keppler H. (2014) Nitrogen speciation in mantle and crustal fluids. *Geochim. Cosmochim. Acta* **129**, 13–32.

Li L., Bebout G. E. and Idleman B. D. (2007) Nitrogen concentration and $\delta^{15}N$ of altered oceanic crust obtained on ODP Legs 129 and 185: insights into alteration-related nitrogen enrichment and the nitrogen subduction budget. *Geochim. Cosmochim. Acta* **71**, 2344–2360.

Li L., Cartigny P. and Ader M. (2009) Kinetic nitrogen isotope fractionation associated with thermal decomposition of NH_3: Experimental results and potential applications to trace the origin of N2 in natural gas and hydrothermal systems. *Geochim. Cosmochim. Acta* **73**, 6282–6297.

Li L., Sheerwood Lollar B., Li H., Wortmann U. G. and Lacrampe-Couloume G. (2012) Ammonium stability and nitrogen isotope fractionations for NH_3(aq)–NH_3(gas) systems at 20–70 °C and pH of 2–13: applications to habitability and nitrogen cycling in low-temperature hydrothermal systems. *Geochim. Cosmochim. Acta* **84**, 280–296.

Li L., Zheng Y.-F., Cartigny P. and Li J. (2014) The nitrogen record of crust-mantle interaction and mantle convection from Archean to present. *Earth Planet. Sci. Lett.* **403**, 67–78.

Li X. and Liu Y. (2011) Equilibrium Se isotope fractionation parameters: a first-principles study. *Earth Planet. Sci. Lett.* **304**, 113–120.

Liu Q., Tossell J. A. and Liu Y. (2010) On the proper use of the Bigeleisen–Mayer equation and corrections to it in the calculation of isotopic fractionation equilibrium constants. *Geochim. Cosmochim. Acta* **74**, 6965–6983.

Liu Y. and Tossell J. A. (2005) Ab initio molecular orbital calculations for boron isotope fractionations on boric acids and borates. *Geochim. Cosmochim. Acta* **69**, 3995–4006.

Martell and Hancock (1996) *Metal Complexes in Aqueous Solutions*. Springer books.

Meek D. W. and Ibers J. A. (1970) Crystal structure of hexaamminecobalt(III) tetrachlorozincate(II) chloride, $[Co(NH_3)_6][ZnCl_4]$ Cl. *Inorg. Chem.* **9**, 465–470.

Meng X. and Han K. N. (1996) The principles and applications of ammonia leaching of metals—a review. *Mineral Processing and Extractive Metullargy Review* **16**, 23–61.

Méheut M., Lazzeri M., Blan E. and Mauri F. (2007) Equilibrium isotopic fractionation in the kaolinite, quartz, water system: Prediction from first-principles density-functional theory. *Geochim. Cosmochim. Acta* **71**, 3170–3181.

Mikhail S. and Sverjensky D. A. (2014) Nitrogen speciation in upper mantle fluids and the origin of Earth's nitrogen-rich atmosphere. *Nat. Geosci.* **7**, 816–819.

Müller T. G. and Kraus F. (2015) Crystal structure of $[Co(NH_3)_6][Co(CO)_4]_2$. *Acta Crystallogr. Sect. E: Crystallogr. Commun.* **71**, 1418–1420.

Nilsson K. B., Eriksson L., Kessler V. G. and Persson I. (2007) The coordination chemistry of the copper(II), zinc(II) and cadmium (II) ions in liquid and aqueous ammonia solution, and the crystal structures of hexaamminecopper(II) perchlorate and chloride, and hexaamminecadmium(II)chloride. *J. Molecular Liquids* **131–132**, 113–120.

Onstott T. C., Lin L.-H., Davidson M., Mislowack B., Borcsik M., Hall J., Slater G., Ward J., Sherwood Lollar B., Lippmann-Pipke J., Boice E., Pratt L., Pfiffner S. M., Moser D., Gihring T., Kieft T. L., Phelps T. J., VanHeerden E., Litthaur D., DeFlaun M., Rothmel R., Wanger G. and Southam G. (2006) The origin and age of biogeochemical trends in deep fracture water of the Witwatersrand Basin, South Africa. *Geomicrobiol. J.* **23**, 369–414.

Paul B., Näther C., Walfort B., Fromm K. M., Zimmermann B., Langc H. and Janiak C. (2004) Molecular paneling of rac-1, 1'-bi-2-naphthol/yate (BINOL/BINOLAT): hydrogen-bonded assembly of [M (NH3) 4 or 6] 2 complexes (M∼ Ni, Zn, Cd) in cavities of {[BINOLAT] 2J (BINOL) 2}-strands. *Cryst. Eng. Comm.* **6**, 293–297.

Pavelka M. and Burda J. V. (2005) Theoretical description of copper Cu (I)/Cu (II) complexes in mixed ammine-aqua environment. DFT and ab initio quantum chemical study. *Chem. Phys.* **312**, 193–204.

Petts D., Chacko T., Stachel T., Stern R. and Heaman L. (2015) A nitrogen isotope fractionation factor between diamond and its parental fluid derived from detailed SIMS analysis of a gem diamond and theoretical calculations. *Chem. Geol.* **410**, 188–200.

Rees C. E. (1973) A teady-state model for sulphur isotope fractionation in bacterial reduction processes. *Geochim. Cosmochim. Acta* **37**, 1141–1162.

Richet P., Bottinga Y. and Javoy M. (1977) A review of hydrogen, carbon, nitrogen, oxygen, sulphur, and chlorine stable isotope

fractionation among gaseous molecules. *Ann. Rev. Earth Planet. Sci.* **5**, 65–110.

Rotzinger F. P. (2009) Investigation of the ligand-field states of the hexaammine cobalt(III) ion with quantum chemical methods. *J. Chem. Theory Comput.* **5**, 1061–1067.

Roy L. E., Hay P. J. and Martin R. L. (2008) Revised Basis Sets for the LANL Effective Core Potentials. *J. Chem. Theory Comput.* **4**, 1029–1031.

Rudolph W. W., Mason R. and Pye C. C. (2000) Aluminium (III) hydration in aqueous solution. A Raman spectroscopic investigation and an ab initio molecular orbital study of aluminium (III) water clusters. *Phys. Chem. Chem. Phys.* **2**, 5030–5040.

Rustad J. R., Casey W. H., Yin Q. Z., Bylaska E. J., Felmy A. R., Bogatko S. A., Jackson V. E. and Dixon D. A. (2010) Isotopic fractionation of Mg 2+(aq), Ca 2+(aq), and Fe 2+(aq) with carbonate minerals. *Geochim. Cosmochim. Acta* **74**, 6301–6323.

Rustad J. R., Nelmes S. L., Jackson V. E. and Dixon D. A. (2008) Quantum-chemical calculations of carbon-isotope fractionation in CO2 (g), aqueous carbonate species, and carbonate minerals. *J. Phys. Chem. A* **112**, 542–555.

Savard M. M., Cole M., Smirnoff A. and Vet R. (2017) $\delta^{15}N$ values of atmospheric N species simultaneously collected using sector-based samplers distant from sources – Isotopic inheritance and fractionation. *Atm. Environ.* **162**, 11–22.

Scalan R. S. (1958) *The Isotopic Composition, Concentration, and Chemical State of the Nitrogen in Igneous Rocks* PhD Thesis. University of Arkansas, Fayetteville.

Schauble E., Rossman G. R. and Taylor H. P. (2004) Theoretical estimates of equilibrium chromium-isotope fractionations. *Chem. Geol.* **205**, 99–114.

Schauble E., Ghosh P. and Eiler J. M. (2006) Preferential formation of ^{13}C–^{18}O bonds in carbonate minerals, estimated using first-principles lattice dynamics. *Geochim. Cosmochim. Acta* **70**, 2510–2529.

Schmiedekamp A. M., Ryan M. D. and Deeth R. J. (2002) Six-Coordinate Co^{2+} with H_2O and NH_3 ligands: Which spin state is more stable? *Inorg. Chem.* **41**, 5733–5743.

Shoeib T., Milburn R. K., Koyanagi G. K., Lavrov V. V., Bohme D. K., Siu K. M. and Hopkinson A. C. (2000) A study of complexes $Mg(NH_3)_n^{+\cdot}$ and Ag (NH_3) $^{+}_{n}$, where n = 1–8: competition between direct coordination and solvation through hydrogen bonding. *Inter. J. Mass Spectrom.* **201**, 87–100.

Sutton, L. E. and Bowen, H. J. M. (1958) Tables of Interatomic Distances and Configuration in Molecules and Ions. Chemical Society, London, Special Publication, no. 11.

Svensen H., Bebout G. E., Kronz A., Li L., Planke P., Chevallier L. and Jamtveit B. (2008) Nitrogen geochemistry as a tracer of fluid flow in a hydrothermal vent complex in the Karoo Basin, South Africa. *Geochim. Cosmochim. Acta* **72**, 4929–4947.

Talbot M. R. and Johannessen T. (1992) A high resolution palaeoclimatic record for the last 27,500 years in tropical West Africa from the carbon and nitrogen isotopic composition of lacustrine organic matter. *Earth Planet. Sci. Lett.* **110**, 23–37.

Thode H. G., Graham R. L. and Ziegler J. A. (1945) A mass spectrometer and the measurement of isotope exchange factor. *Can. J. Res.* **B23**, 40–47.

Urey H. C. (1947) The thermodynamic properties of isotopic substances. *J. Chem. Soc.*, 562–581.

Urey H. C. and Aten A. H. W. (1936) On the chemical differences between nitrogen isotopes. *Phys. Rev.* **50**, 575.

Valli M., Matsuo S., Wakita H., Yamaguchi T. and Nomura M. (1996) Solvation of copper(II) ions in liquid ammonia. *Inorg. Chem.* **35**, 5642–5645.

Varadwaj P. R., Cukrowski I. and Marques H. M. (2008) DFT-UX3LYP studies on the coordination chemistry of Ni^{2+}. Part 1: Six coordinate $[Ni(NH_3)_n(H_2O)_{6-n}]^{2+}$ complexes. *J. Phys. Chem. A* **112**, 10657–10666.

Varadwaj P. R., Cukrowski I. and Marques H. M. (2009) Low-spin complexes of Ni^{2+} with six NH_3 and H_2O ligands: A DFT–RX3LYP study. *J. Mol. Struct. (THEOCHEM)* **902**, 21–32.

Varadwaj P. R. and Marques H. M. (2010) The physical chemistry of coordinated aqua-, ammine-, and mixed-ligand Co^{2+} complexes: DFT studies on the structure, energetics, and topological properties of the electron density. *Phys. Chem. Chem. Phys.* **12**, 2126–2138.

Wahl M. H., Huffman J. F. and Hipple J. A. (1935) An attempted concetration of the heavy nitrogen isotope. *J. Chem. Phys.* **3**, 434–435.

Walters W. W., Chai J. and Hastings M. G. (2019) Theoretical phase resolved ammonia−ammonium nitrogen equilibrium isotope exchange fractionations: Applications for tracking atmospheric ammonia gas-to-particle conversion. *ACS Earth Space Chem.* **3**, 79–89.

Wheat C. G., Fryer P., Fisher A. T., Hulme S., Jannasch H., Mottl M. J. and Becker K. (2008) Borehole observations of fluid flow from South Chamorro Seamount, and active serpentinite mud volcano in the Mariana forearc. *Earth Planet. Sci. Lett.* **267**, 401–409.

Widmer-Cooper A. N., Lindoy L. F. and Reimers J. R. (2001) The effect of alkylation of N-and O-donor atoms on their strength of coordination to silver (I). *J. Phys. Chem. A* **105**, 6567–6574.

Williams A. F. (1979) *A theoretical approach to inorganic chemistry*. Springer-Verlag, Berlin, p. 318. https://doi.org/10.1007/978-3-642-67117-3.

Young E. D., Manning C. E., Schauble E. A., Shahar A., Macris C. A., Lazar C. and Jordan M. (2015) High-temperature equilibrium isotope fractionation of non-traditional stable isotopes : Experiments, theory, and applications. *Chem. Geol.* **395**, 176–195.

Zeng T., Lancaster K. M., Ananth N. and Hoffmann R. (2015) Anomalous orbital admixture in ammine complexes. *J. Organometal. Chem.* **792**, 6–12.

Zhang S. and Liu Y. (2014) Molecular-level mechanisms of quartz dissolution under neutral and alkaline conditions in the presence of electrolytes. *Geochemical J.* **48**, 189–205.

Zhang Y. N. and Liu Y. (2018a) The theory of equilibrium isotope fractionations for gaseous molecules under super-cold conditions. *Geochim. Cosmochim. Acta.* **238**, 123–149.

Zhang J. and Liu Y. (2018b) Zinc isotope fractionation under vaporization processes and in aqueous solutions. *Acta Geochim.* **37**, 663–675.

Associate editor: Marc Blanchard